Department of Advanced Materials Science,
School of Frontier Sciences,
The University of Tokyo

Master thesis

Structure and dynamics of silica nanoparticles in liquid crystal investigated with synchrotron x-ray radiation

放射光 X 線を用いた液晶中のシリカ・ナノ粒子の構造とダイナミクスの研究

Submitted on July 12th, 2011
Supervisor：Professor Yoshiyuki Amemiya

47-096124：Xu Zhong (仲　旭)

平成二十三年度修士論文　放射光X線を用いた液晶中のシリカ・ナノ粒子の構造とダイナミクスの研究　仲　旭

Abstract

Silica nanoparticles with diameter around 100 nm were dispersed into a nematic liquid crystal 5CB with different volume fractions φ. Differential scanning calorimetry (DSC) was performed to study the nematic to isotropic transition temperature of these nematic liquid crystal colloids. Small angle x-ray scattering (SAXS) was performed to study the structure of silica nanoparticles dispersed in 5CB. Microbeam wide angle x-ray scattering (microbeam WAXS) was performed to study the structure of 5CB in which silica nanoparticles were dispersed. X-ray photon correlation spectroscopy (XPCS) experiment was performed to study the dynamics of silica nanoparticles dispersed in 5CB. DSC reveals that the nematic to isotropic transition temperature of 5CB decreases linearly with increasing φ. SAXS shows that silica nanoparticles contact with each other in these nematic liquid crystal colloids. Microbeam WAXS indicates that 5CB molecules become less oriented with increasing φ, and the peak of scattering profile becomes broader with increasing φ. XPCS shows that relaxation time of these samples increases with increasing φ, and a transition from a stretched exponential behavior for φ equal to 0.3 % to a compressed exponential behavior for φ equal to 5.0 % has been observed. A detailed discussion on experimental results will be given in this thesis.

Keywords：nematic liquid crystal colloid，anisotropic structure, dynamics, SAXS, Microbeam WAXS, XPCS.

Acknowledgments

Much appreciation goes to people who have been helping and supporting me during these two years, and it is their contributions that ensured the study and experiments mentioned in this thesis.

First of all, I'd like to thank my advisor, Professor Y. Amemiya, who has really treated me well and helped me a lot in developing my research capacity. His abundant knowledge, intuition and experience on x-ray scattering have made him an expert of this field and have taught me to seek in the right direction more rigorously and critically. He also taught me a lot during daily conversation on philosophy of life, and his passion and curiosity on many unknown issues really impress me.

Furthermore, I'm deeply grateful to Dr. Y. Shinohara, the assistant professor of Amemiya lab. He helped me a lot to build the experimental set up during the experiments at synchrotron facilities and instructed me how to take and analyze data correctly. Discussing with him is always beneficial to me on how to process and modify my study. His intelligence, diligence, enthusiasm and persistence on academic exploration impress me a lot.

Besides, I really appreciate Dr. Y. Ueji, Dr. Y. Nozue, Dr. H. Kishimoto, Dr. G. Tamura, K. Yamazoe, S. Tsuji, M. Handa, I. Inoue and H. Seike, former or current members of Amemiya Lab for their support during the experiments and for their useful advices and discussions on my study.

Special thanks goes to Mrs. S. Kawajiri, the secretary of Amemiya lab, for her sincere and gentle help and support from the first day I came here to Kashiwa campus and throughout my study here for two years.

Also, I'd like to thank Dr. N. Ohta, Dr. A. Iida and Dr. H. Masunaga and other relevant beam line scientists at Spring-8 and Photon Factory for their technical assistance with the experiments.

Finally, I must thank my family and loving parents. During the last several years, seldom did I have chance to stay home, as the only child of my family, I must express my appreciation for their continuous support and understanding.

The experiments were performed under the approval of PF-PAC (Proposal No. 2010G526) and JASRI (Proposal Nos. 2010B7264, 2010B1196).

Contents

1 Introduction

Nematic liquid crystal is anisotropic at its nematic phase and can serve as an anisotropic matrix for colloidal dispersions. This can generate distinct physical phenomenon compared to isotropic surrounding matrices.

Topological defects will occur when colloidal particles are dispersed into nematic liquid crystal. Some typical topological defects have already been theoretically estimated and experimentally observed [5, 6, 19-22]. Short range repulsive and long range attractive forces exist among topological defects. Under these forces, self-assemble anisotropic structures can be formed. The typical anisotropic structures include linear structure [21, 23, 24], hexagonal structure [25, 26], multiple structure [9] and cellular structure [14, 27-30]. Properties of nematic liquid crystal colloids have also been investigated such as dielectric property [31], optical property [32], thermal property [30, 33] and mechanical property [14, 30].

So far, the structures of nematic liquid crystal colloids were mainly investigated under optical microscope. Because of the resolution limitation of optical microscope, the samples were fabricated to be very thin in the range of several tens of microns.

To conquer this limitation, here in this study, much thicker samples with thickness around 1 mm were studied with synchrotron x-ray radiation.

In detail, small angle x-ray scattering has been performed to study the structures of silica nanoparticles dispersed in a nematic liquid crystal 5CB. Microbeam wide angle x-ray scattering has been performed to investigate the structure and orientation change of 5CB molecules. X-ray photon correlation spectroscopy has been performed to study the dynamics of dispersed silica nanoparticles.

In this master thesis, chapter 2 gives an introduction of the background of this study, that is colloidal dispersions in nematic liquid crystal. Chapter 3 summarizes the basics of x-rays and x-ray scattering. Chapter 4 introduces the experimental study of structure and dynamics of silica nanoparticles dispersed in 5CB. Chapter 5 gives a summary of this thesis.

2 Colloidal dispersions in nematic liquid crystal

Colloidal dispersions are particles with sizes from 10 nm to 10 μm dispersed in a surrounding matrix. It can be commonly found in nature, in daily life, in industrial products and is also of remarkable academic and technological importance. Academically, colloidal dispersions are ideal systems to investigate Brownian motion and hydrodynamic interactions of suspended particles [1, 2]. Technologically, colloidal dispersions are indispensable in manufacturing drugs, cosmetics etc.

In most cases, colloidal particles are dispersed in isotropic matrices, thus the consequent optical, electric, mechanical properties of the colloidal dispersion are usually isotropic.

Here in the section, we will focus on a different question of how the colloidal particles behave when dispersed in an anisotropic matrix. For simplicity, we will introduce the nematic liquid crystal as the anisotropic matrix.

2.1 Phenomenological description of nematic liquid crystal

Nematic liquid crystals are usually rodlike organic molecules aligning on average along a unit vector **n**, called the Frank director [3], at their nematic phase. The directors form a uniform director field throughout space. When temperature is increased above certain critical temperature defined as nematic to isotropic transition temperature, the nematic liquid crystal will turn to isotropic phase with director **n** orienting randomly without any long range positional and orientational order. The phase transition can be illustrated by figure 2.1.

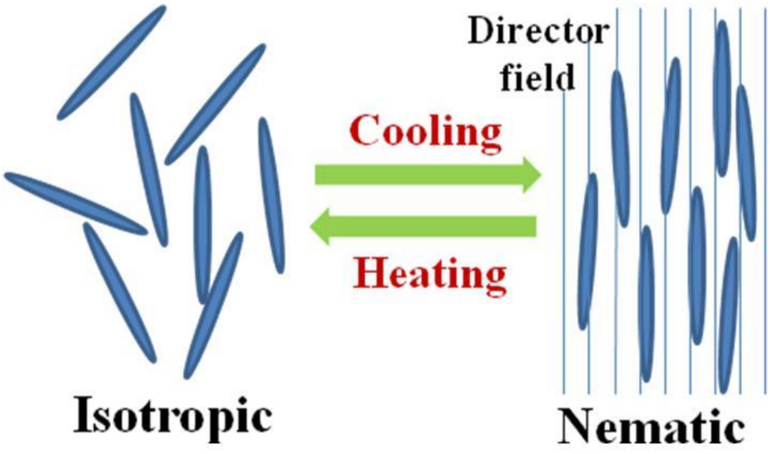

Fig.2.1 Phase transition between nematic and isotropic for nematic liquid crystal.

When particles are dispersed into nematic liquid crystal, liquid crystal molecules surrounding the particles will anchor to particles. Correspondingly the surrounding director field will be elastically distorted, which will result in topological defects. Among these topological defects, there will be short range repulsive and long range attractive interactions. These interactions will finally generate distinctive structures and dynamics of the colloidal particles, compared to the cases when the matrices are isotropic.

2.1.1 Frank free energy and surface anchoring energy

From thermodynamics we know that a system on a macroscopic level has the tendency to minimize its thermodynamic potential. Before describing energy of nematic liquid crystal, we want to mention that the Frank director **n**(**r**), which specifies the direction of local alignment of anisotropic liquid crystal molecules at the point r, is invariant under the inversion operation **n**(**r**)→**n**(-**r**).

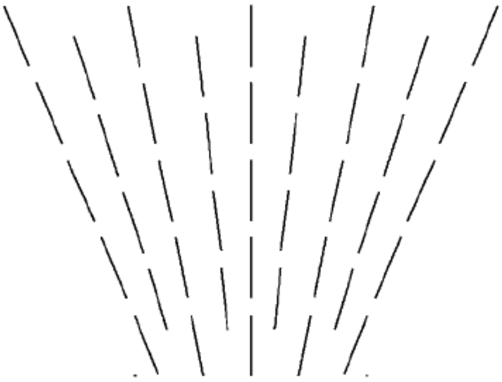

Splay: K_1

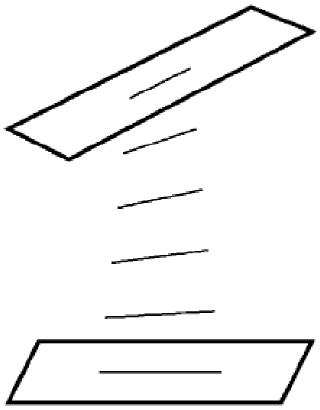

Twist: K_2

Bend: K_3

Fig. 2.2 Illustration of deformation of nematic liquid crystals [4].

Let's consider the free energy of nematic liquid crystal, no matter it is pure or it has been dispersed with colloidal particles. The energetic ground state of a nematic liquid crystal is a spatially uniform director field and any deviation from it costs elastic energy. The elastic distortions in a nematic liquid crystal are known as splay, twist and bend deformations [4] as figure 2.2 shows. The resultant Frank free energy density f is [5, 6]

$$f(\mathbf{r}) = \frac{1}{2}K_1(\nabla\cdot\mathbf{n})^2 + \frac{1}{2}K_2(\mathbf{n}\cdot\nabla\times\mathbf{n})^2 + \frac{1}{2}K_3[\mathbf{n}\times(\nabla\times\mathbf{n})]^2\,, \tag{2.1}$$

where K_1, K_2 and K_3 are the splay, twist and bend moduli, respectively.

Theoretically, the Frank free energy F can be determined by integrating over the volume and the minimum of F can be obtained under appropriate boundary conditions. An exact calculation is very difficult and is beyond introduction of this section. For simplicity, based on an analog to the electrostatics [7, 8], a one-constant approximation can be applied. That is to set K_1=K_2=K_3=K. Under this approximation, Frank free energy density f can be written as [10]

$$f(\mathbf{r}) = \frac{K}{2}[(\nabla\cdot\mathbf{n})^2 + (\nabla\times\mathbf{n})^2]\,. \tag{2.2}$$

The free energy F can be reduced to [6, 9]

$$F = \frac{K}{2}\sum_{i,j}\int d^3r(\nabla_i n_j)^2\,, \tag{2.3}$$

where the integral is over the volume of the nematic liquid crystal; $i, j=x, y, z$; n_i is the i^{th} component of the director, $\nabla_i n_j$ is the gradient of n_j, and $\nabla_i = \partial / \partial x_i$.

Dispersing colloidal particles into nematic liquid crystal will generate interface between particles and liquid crystal molecules, and the resultant surface free energy density at the surface element S of the particle is given by [11-13]

$$f_s(S) = \frac{W}{2}[1-(\mathbf{n}\cdot\mathbf{v})^2], \tag{2.4}$$

where W is the coupling constant or the surface anchoring constant, **v** is the unit vector normal to the colloid surface.

For a given particle configuration, the total free energy including both Frank free energy F and surface free energy F_s can be expressed as

$$F(\mathbf{n}(\mathbf{r})) = F + F_s = \int d\mathbf{r} f(\mathbf{r}) + \oint dS f_s(S). \tag{2.5}$$

The increase of Frank free energy intends to expel colloidal particles away from nematic liquid crystal matrix while the increase of surface free energy has the inclination to stable the particles. The director field around such a particle is controlled by the competition between the surface free energy or surface anchoring energy at the interface and the Frank free energy or Frank elastic energy in the bulk.

A scaling argument tells us $F \propto KR$ and $F_s \propto WR^2$. W is typically of the order W~10^{-6} J/m2 and K~10^{-11} J/m [3, 17].

A critical radius of colloidal particles can be obtained by setting F equal to F_s, that is ξ_c given by

$$\xi_c = \frac{K}{W}. \tag{2.6}$$

Suppose a particle of radius R in a nematic environment with a uniform director field at infinity, the Frank free energy of this system is proportional to KR while the surface energy is proportional to WR^2. Taking normal boundary condition for example, for strong anchoring, that is $WR^2 >> KR$, or equivalently $R>>\xi_\mathrm{c}$, the energy to turn the director to **v** at the whole surface would be much larger than the bulk energy. Under this condition, it is preferable for the system that the director points along **v** nearby the interface. On the contrary, for weak anchoring, that is $WR^2 << KR$, or equivalently $R<<\xi_\mathrm{c}$, the influence of the surface is minor, that the director may have a divergence from the original director field but will not be along the direction of **v**.

2.1.2 Miesowics viscosities

In the previous subsections, we mainly described the static properties of director field by considering Frank elastic energy and surface anchoring energy. Here the viscosity of nematic liquid crystal will be briefly introduced.

Liquid crystal hydrodynamics has been studied for a long time. The detailed hydrodynamic equations can be found in several references such as [3, 15]. Here we will not focus on hydrodynamic equations but on viscosity of nematic liquid crystal. For isotropic matrices, the viscosity is usually isotropic. Nematic liquid crystal is anisotropic at its nematic phase, resulting in anisotropic viscosities called Miesowics viscosities [16-18] as figure 2.3 shows [6].

The direct field between the upper and lower plates is spatially uniform, and the upper plate is moved with a velocity v_0 relative to the lower one, creating a constant velocity gradient along the vertical z direction. The director **n** can be aligned in one direction by applying a magnetic field strong enough to exceed the viscous torques. During measurement, **n** is controlled either parallel to velocity **v** or perpendicular to **v** and its gradient, or perpendicular to **v** but parallel to its gradient.

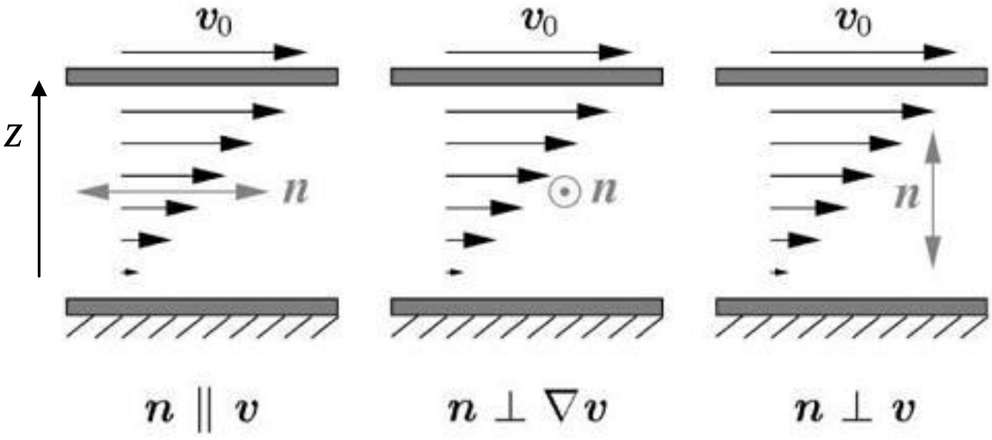

Fig. 2.3 Definition of three Miesowics viscosities in shear experiments [6].

2.2 Topological defects

2.2.1 Expected topological defects

Topological defects are necessary consequence of broken continuous systems. For pure nematic liquid crystal, the director field is continuous within the liquid crystal, but it will be influenced more or less after being dispersed by colloidal particles. As a result, the topological defects are to be formed. Topological conservation law tells us that the director field of nematic liquid crystal should be continuous, which determines the possible configuration of topological defects around the dispersed colloidal particles.

Particles are pretreated with surfactants before being dispersed into nematic liquid crystal to decrease surface energy in order to make it easier to disperse the particles. Here we just consider two typical cases: one with normal boundary condition, the other with planer boundary condition.

Planer boundary condition means that nematic liquid crystal molecules should array parallel to the colloidal particle surface under the effect of surfactants. For example, polymers such as polyvinyl alcohol (PVA) provide planar anchoring of thermotropic liquid crystals at water interfaces [19].

Under planer boundary condition, a topological defect is expected as depicted by figure 2.4 [5, 20].

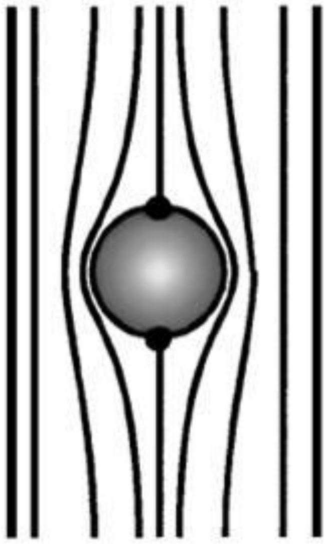

Fig. 2.4 Topological defect under planer boundary condition [5].

For topological defects under normal boundary conditions, things become more complicated, because as illustrated in the previous subsection, the configuration is under the competition between Frank elastic energy and surface anchoring energy. A sphere particle with normal boundary condition can be depicted as figure 2.5, nematic liquid crystal molecules should array normal to the colloidal particle surface under the effect of surfactants [5].

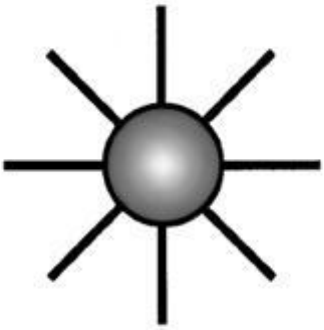

Fig. 2.5 A sphere particle with normal boundary condition [5].

For weak anchoring, that is $WR^2 << KR$, or equivalently $R<<\xi_c$, the influence of the surface is minor. The director may have a divergence from the original director field but will not be along the direction of **v**. In this case, the director adjacent to the particle can be expected as figure 2.6 shows [6].

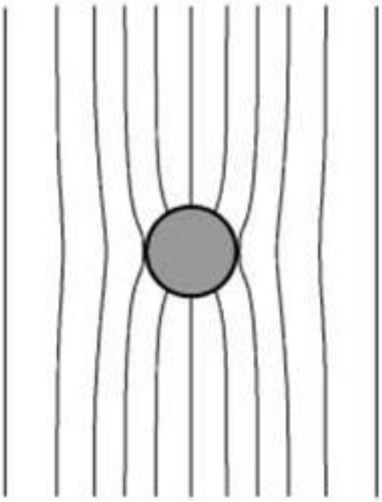

Fig. 2.6 Topological defect under weak normal boundary condition [6].

For strong anchoring, that is $WR^2 >> KR$, or equivalently $R>>\xi_c$, the energy to turn the director to **v** at the whole surface would be much larger than the bulk energy. Under this condition, it is preferable for the director to point along **v** nearby the interface. Two types of topological defects, called hyperbolic hedgehog defect and Saturn ring defect, respectively, as illustrated by figure 2.7 and 2.8, can be expected [6].

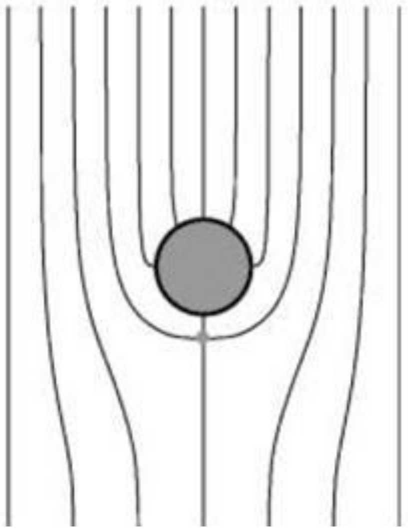

Fig. 2.7 Hyperbolic hedgehog defect [6].

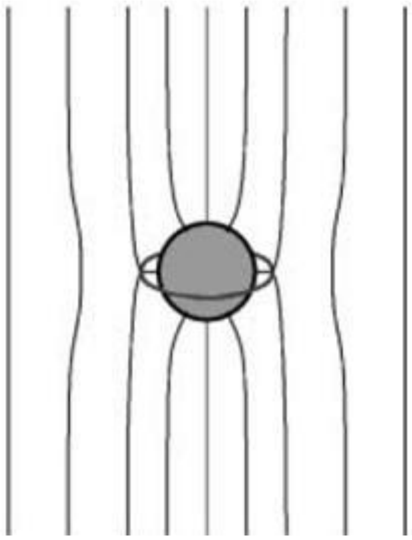

Fig. 2.8 Saturn ring defect [6].

2.2.2 Experimental observation

Experimentally the mentioned topological defects have been investigated successfully. In most of those experiments, the surface of the glass substrates was treated with polyimide and was unidirectionally rubbed to induce good planer anchoring at the surface and parallel alignment of nematic liquid crystal [21]. The nematic liquid crystal colloids were injected into the thin cells made of pretreated glass substrates. The nematic emulsions were observed with polarized optical microscope. Between crossed polarizers, an isotropic region will appear black, whereas nematic regions will be colored thus can be seen [9].

Topological defect under planer boundary condition is shown in figure 2.9 [5]. In this experiment, water was dispersed into ZLI, a nematic liquid crystal, under the surfactant PVA. The thickness of the sample was about 30 μm. The nematic liquid crystal matrix was horizontally aligned. The two bright regions located on the surface of the droplet indicate the presence of surface defects.

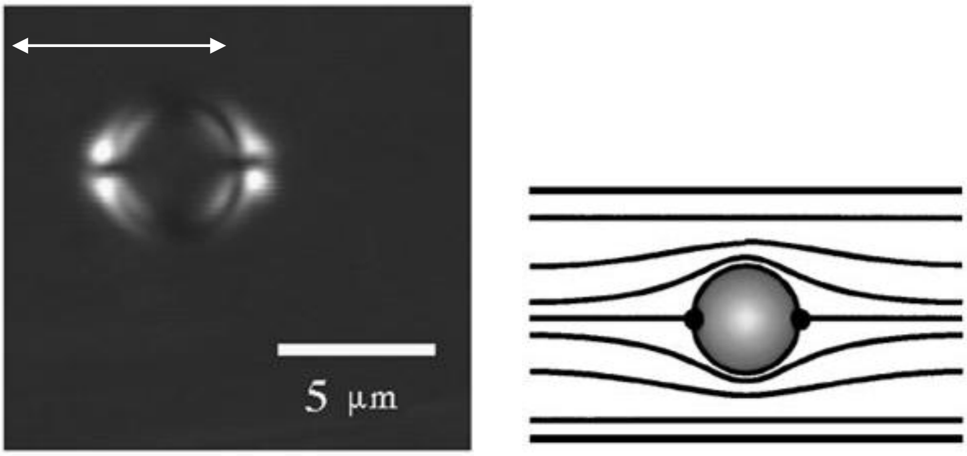

Fig. 2.9 Left: Topological defect under planer boundary condition observed under polarized optical microscope [5]. Right: Expected topological defect.

For normal boundary conditions, water was dispersed into 5CB and K15 under the surfactant Tween 60. The experiment condition was the same as mentioned in the previous subsection on topological defect under planer boundary condition. A hyperbolic hedgehog defect under strong normal boundary condition was observed [5] as figure 2.10 shows.

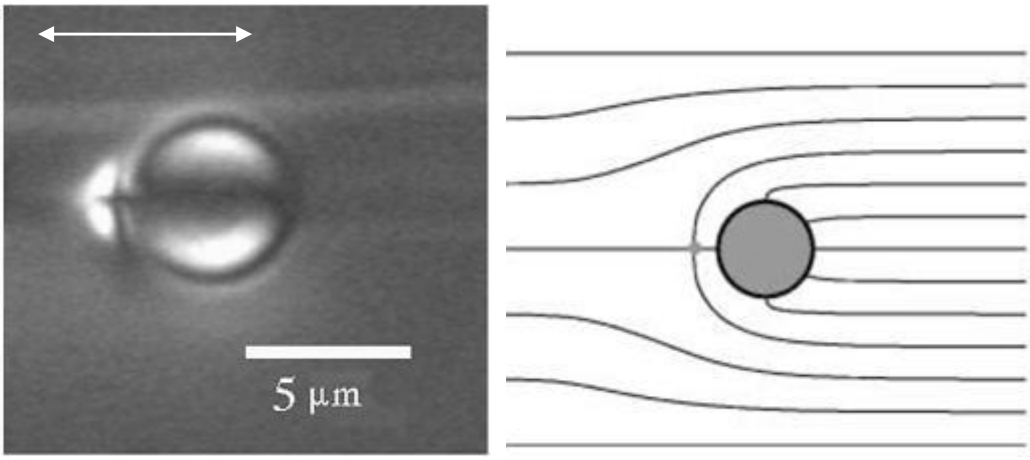

Fig. 2.10 Left: Experimental hyperbolic hedgehog defect under strong normal boundary condition [5]. Right: Expected topological defect.

Saturn ring defect was predicted by topological conservation law, but in actual experiments, hyperbolic hedgehog defect is commonly observed, which confirms that under most experimental conditions, the hyperbolic hedgehog, rather than the Saturn ring defect, is the lowest-energy defect of an isolated particle in homogeneously aligned liquid crystal.

To obtain Saturn ring defect, a thin glass cell with thickness varying along the direction of rubbing. The cells were prepared using mylar spacers on one edge and no spacer on the other edge with thickness varying between 1-6 μm along the direction of rubbing. Silica colloids with diameter 2.32±0.02 μm were coated with a monolayer of DMOAP that ensures very strong perpendicular surface anchoring of the nematic liquid crystal 5CB. At the position within thick 5CB layer, hyperbolic hedgehog defect was observed, whereas at a thin 5CB layer (2.5 μm), Saturn ring defect was successfully detected [21] as figure 2.11 shows. Note that rubbing direction is vertical in this figure. The two black spots on the right and left side of the colloid represent the Saturn ring.

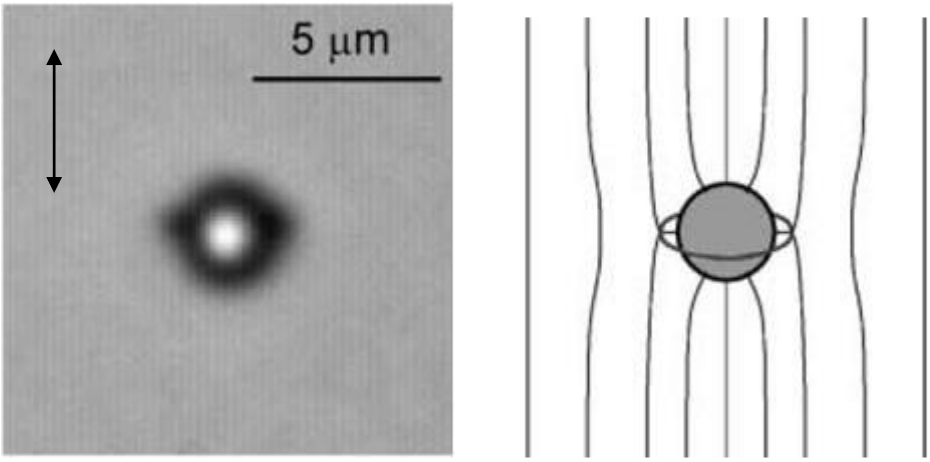

Fig. 2.11 Left: Experimental Saturn ring defect under strong normal boundary condition [21]. Right: Expected topological defect.

Colloidal particles with other shapes but not sphere have also been investigated. C. P. Lapointe et al. [22] fabricated triangular, square and pentagonal colloids using photolithography. All the colloids have a thickness of 1μm while the cells have thickness 10-60 μm. The lateral edge lengths of triangles, squares and pentagons are 3.0 μm, 4.5 μm and 1.5 μm, respectively. The square-shaped particles contain a square hole with 2μm sides. Observed patterns as well as schematics of expected topological defects are shown by figure 2.12, 2.13 and 2.14. Colloidal polygons with an odd number of sides form elastic dipoles, whereas even-sided particles form elastic quadrupoles.

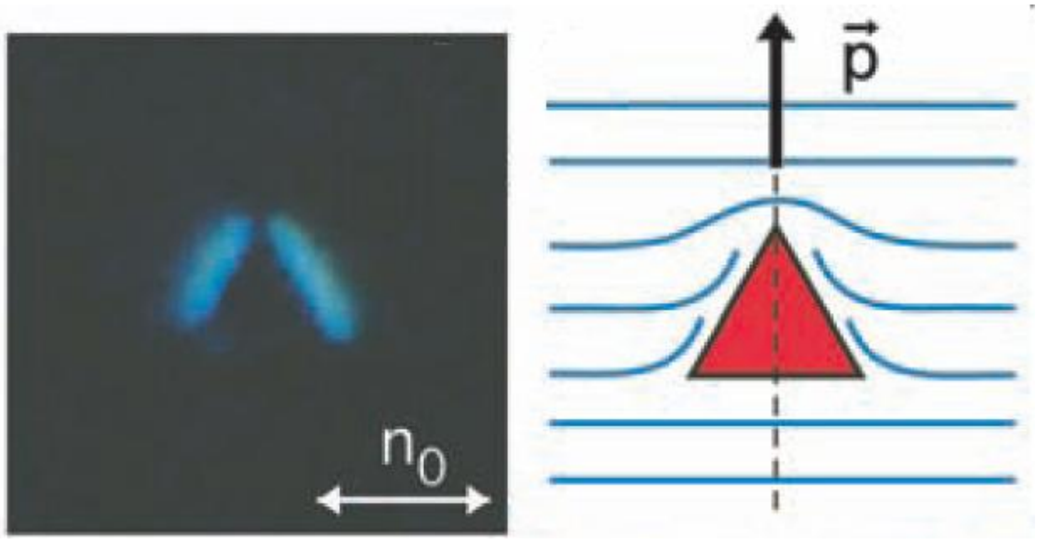

Fig. 2.12 Topological defect of triangular colloids [22].

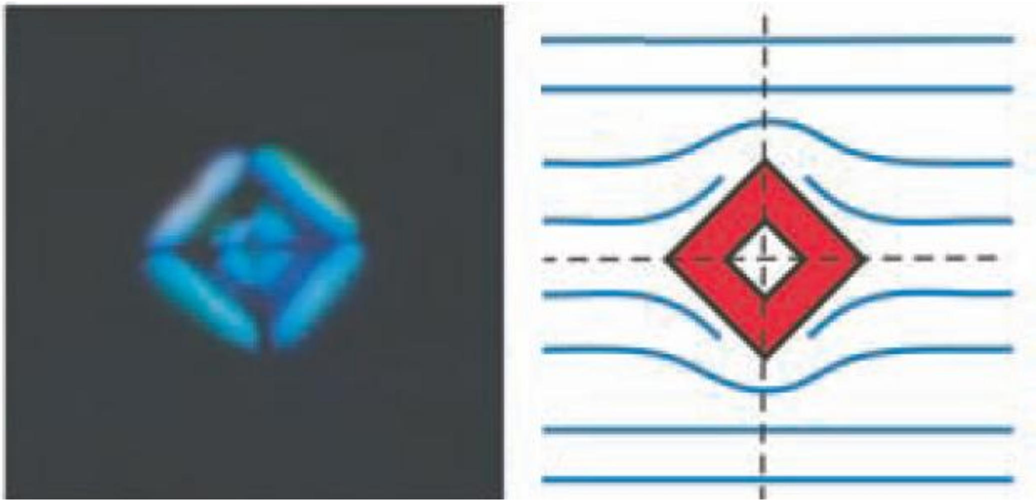

Fig. 2.13 Topological defect of square colloids [22].

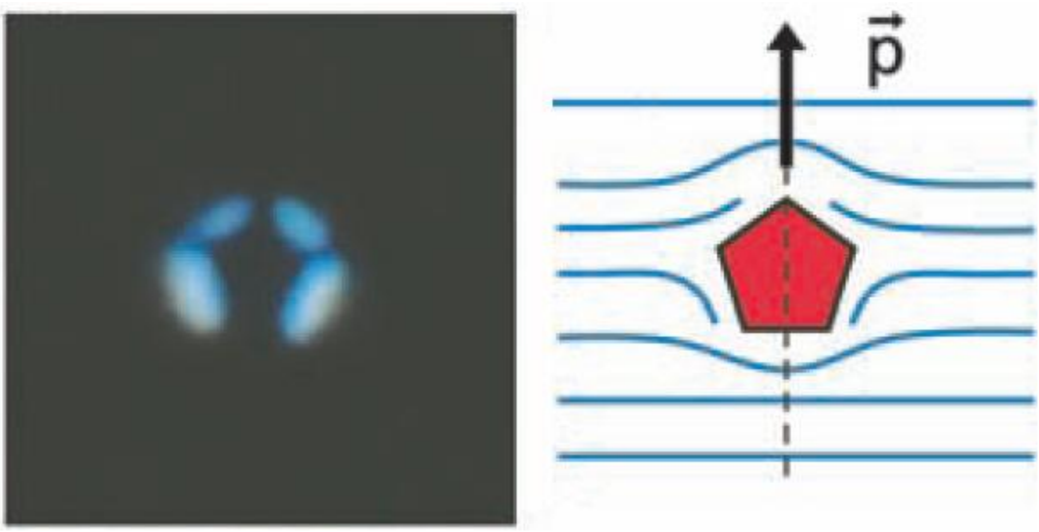

Fig. 2.14 Topological defect of pentagonal colloids [22].

2.3 Self-assembled anisotropic structures

Long range attractive and short range repulsive forces exist among the topological defects, resulting in various anisotropic structures of the colloidal particles. Linear structures are the commonly observed one. Saturn ring defects are analogous to quadrupoles, whereas hyperbolic hedgehog defects are similar to dipoles. The resultant linear structures are different. Hyperbolic hedgehog defects formed linear structures parallel to the rubbing direction, while Saturn ring defects formed jagged lines along the direction perpendicular to the rubbing direction [21] as shown in figure 2.15 and 2.16, respectively. In these two cases, rubbing direction is along the vertical direction from the bottom up.

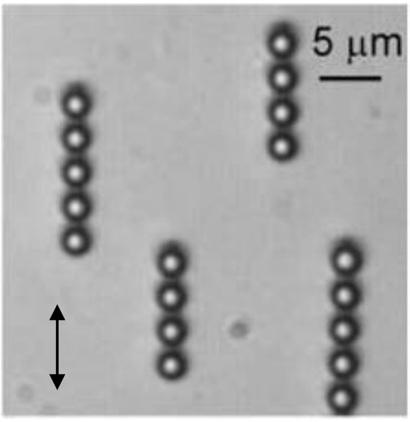

Fig. 2.15 Linear structure along rubbing direction formed by hyperbolic hedgehog effects [21].

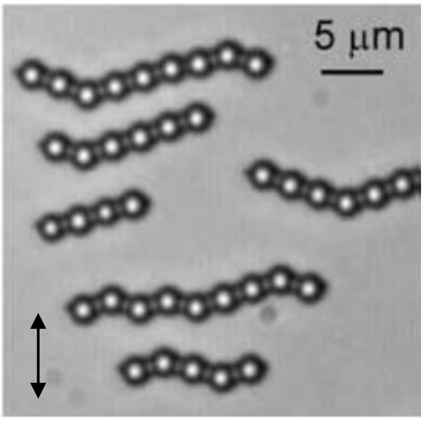

Fig. 2.16 Jagged lines along the direction perpendicular to rubbing direction formed by Saturn ring effects [21].

Linear structures were also observed in other systems. Figure 2.17 shows silicone oil (poly-(dimethylsiloxane-*co*-methylphenylsiloxane)) dispersed in a eutectic mixture of cyanobiphenyl and cyanoterphenyl molecules with the trade name “E7”. Weight fraction of silicone oil is 2.0 % [23, 24].

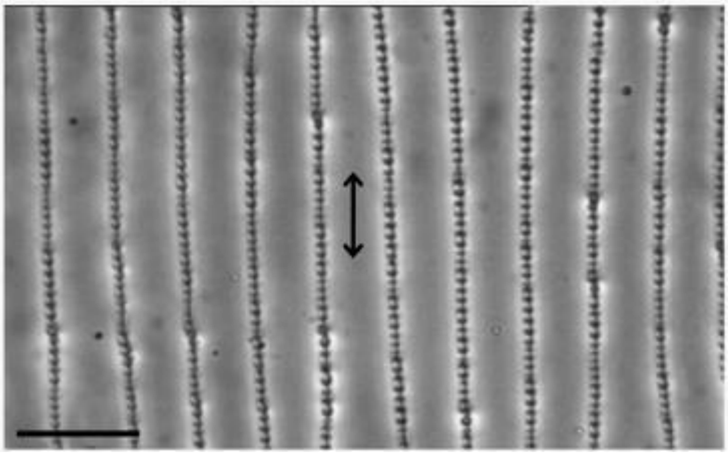

Fig. 2.17 Linear structure of silicone oil dispersed in E7. Black arrow: rubbing direction. Scale bar: 50 μm [23].

Hexagonal structures were also observed by dispersing glycerol into 5CB [25, 26]. Figure 2.18 shows the formed hexagonal structure and figure 2.19 shows a schematic representation.

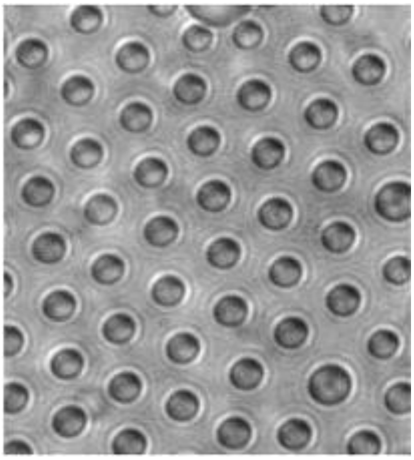

Fig. 2.18 Glycerol forms hexagonal structure in 5CB [25].

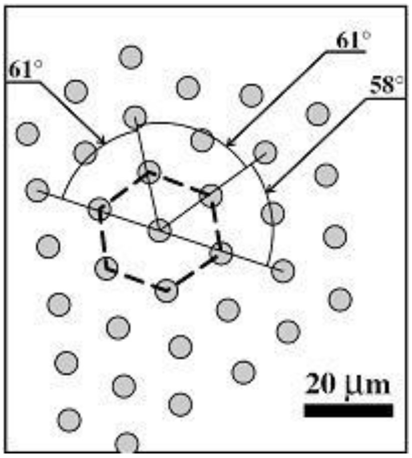

Fig. 2.19 Schematic representation of glycerol structures [25].

A combination of linear structure and cellular structure was observed by dispersing water into 5CB with a normal boundary condition under the surfactant sodium dodecyl sulfate [9]. The water droplets form linear structure within the 5CB, and 5CB was confined in cellular structures formed by water, resulting in a multiple nematic emulsion as figure 2.20 shows.

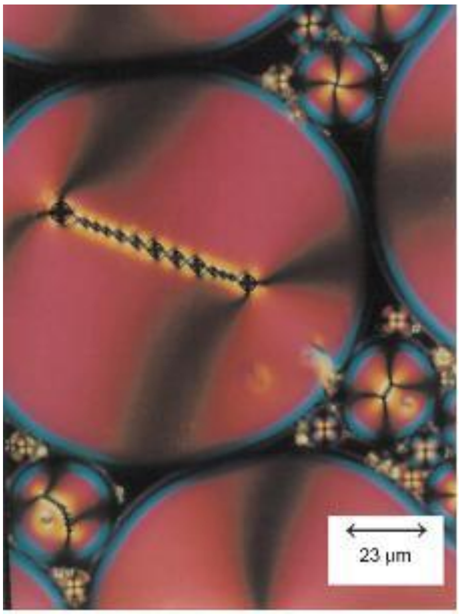

Fig. 2.20 A multiple nematic emulsion formed by dispersing water into 5CB [9].

When the weight fraction or volume fraction of colloidal particles became comparatively large to several percent, cellular structures were reported [14, 27-30]. Figure 2.21 shows a cellular structure by dispersing PMMA nanoparticles (5.0 wt %) into 5CB with the surfactant poly-12-hydroxystearic acid (PHSA) [14].

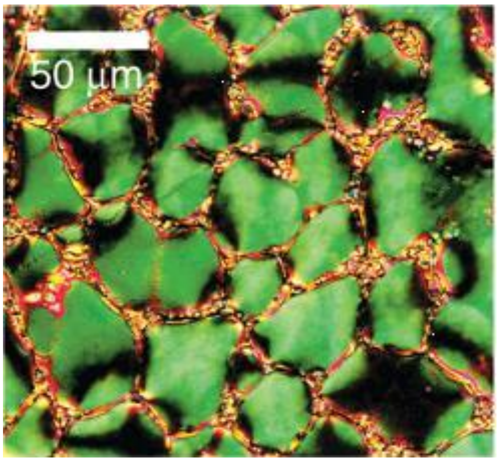

Fig. 2.21 Cellular structure formed by dispersing PMMA nanoparticles into 5CB [14].

The average size of the formed cellular structures has a dependence on concentration on colloidal particles. As shown in figure 2.22, reflection-mode confocal images of cellular structures of PMMA (*d*=150 nm, coated with PHSA) dispersed in 5CB at different concentrations are presented. The average size decreases with increasing concentration as illustrated in figure 2.23 [30].

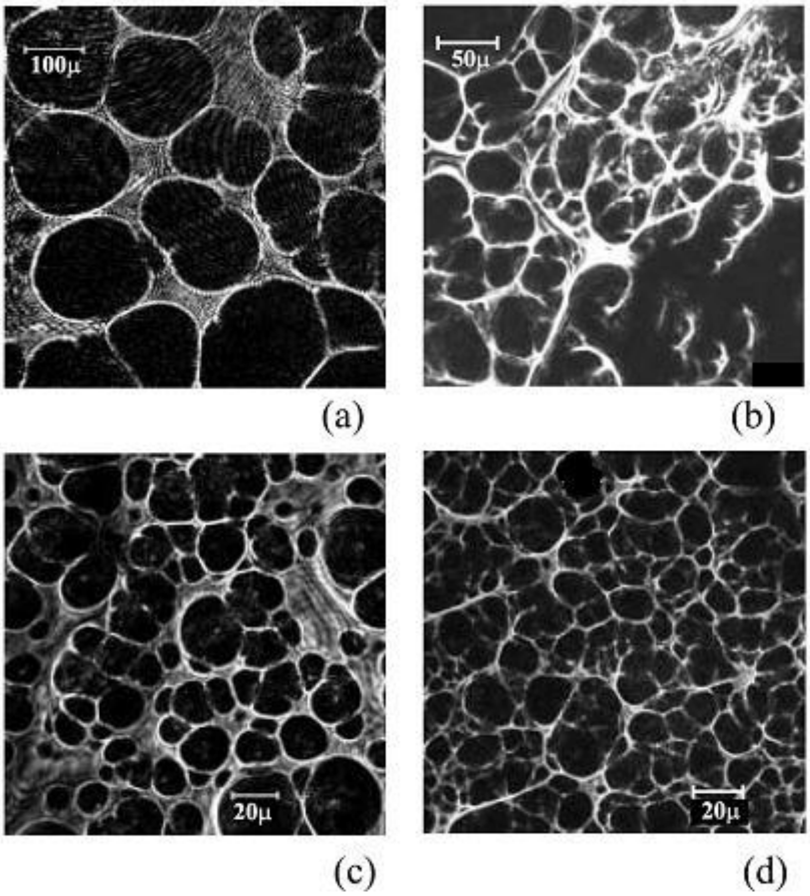

Fig. 2.22 Cellular structures of PMMA dispersed in 5CB at concentrations 3 % (a), 7 % (b), 10 % (c) and 15 % (d) [30].

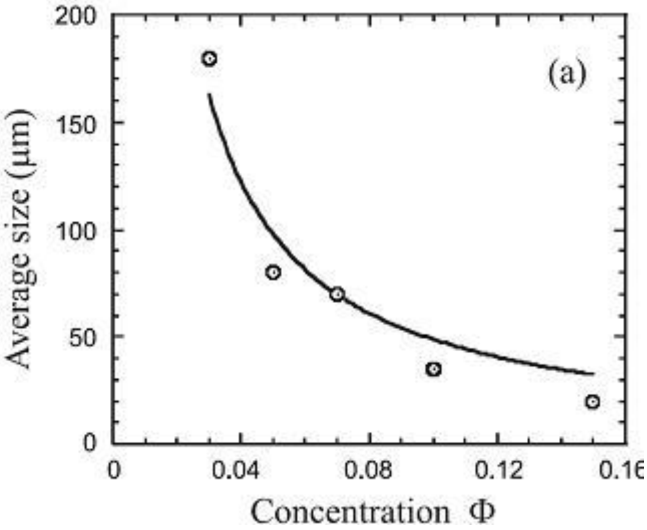

Fig. 2.23 Dependence of average size on PMMA particle concentration [30].

2.4 Properties of nematic liquid crystal colloids

Dielectric properties can be changed by dispersing colloidal particles into nematic liquid crystal. Table 2.1 shows the comparison of permittivity for 5CB containing silica nanoparticles at different weight fractions [31]. The primary particle size is 30-80 nm and the alternating current frequency is 10^5 Hz. Both nematic (T=295 K) and isotropic (T=328 K) phased were measured. At nematic phase, permittivity decreased after silica nanoparticles were added, and the authors explained this phenomenon by mentioning that this behavior is attributed to the influence of the filler particles on the orientation order of the domains in the nematic phase and that the molecules at the surface of the filler are not free to rotate.

Table 2.1 Permittivity of 5CB containing silica nanoparticles [31]

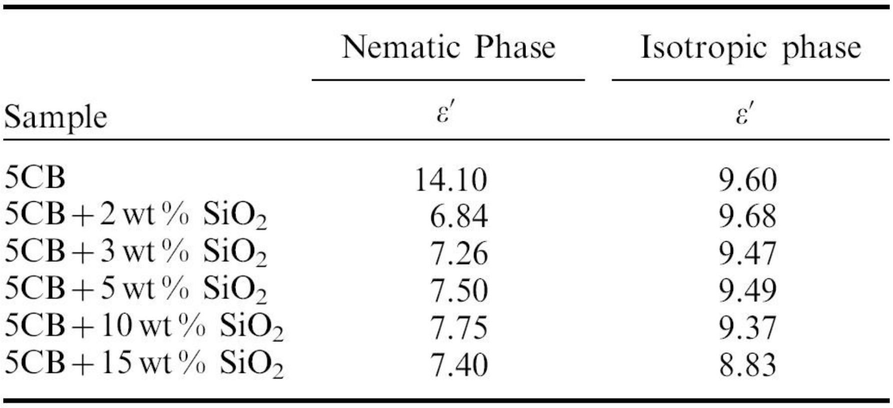

	Nematic Phase	Isotropic phase
Sample	ε'	ε'
5CB	14.10	9.60
5CB + 2 wt % SiO_2	6.84	9.68
5CB + 3 wt % SiO_2	7.26	9.47
5CB + 5 wt % SiO_2	7.50	9.49
5CB + 10 wt % SiO_2	7.75	9.37
5CB + 15 wt % SiO_2	7.40	8.83

Optical properties were measured by S. B. Lee et al [32]. The nematic liquid crystal mixtures BL011 and BL035 were used. The silica nanoparticles (d=40 nm) were dispersed at a concentration of 10-18 wt %. The sample transmittance ($T=I_{out}/I_{in}$) was measured using He-Ne laser as a light source and a photodiode for detection of transmitted light. Transmittance-voltage (T-V) dependence of filled nematic cell was measured as figure 2.24 shows. The memory parameter M was calculated from the ratio $M=(T_r-T_0)/(T_s-T_0)$, where T_0 is the initial transmittance, T_r is the remained transmittance and T_s is the saturated transmittance. The strong memory effect (M≈95 %) was observed and there is a threshold voltage for memory effect, which is about 50-100 V depending on concentration of particles.

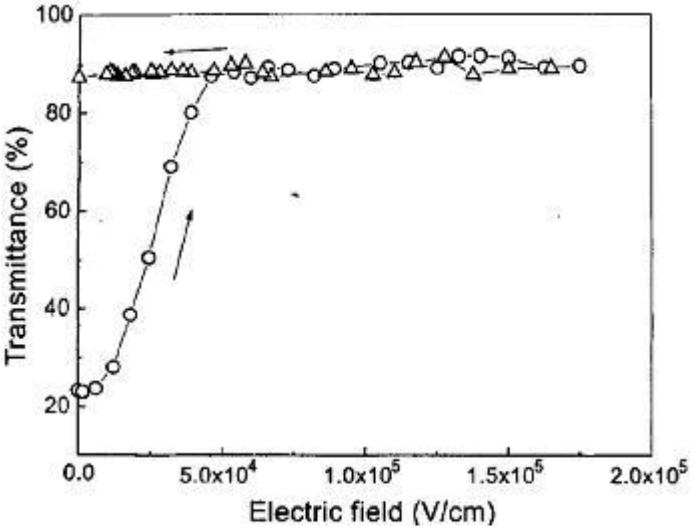

Fig. 2.24 Transmittance-Voltage dependence of nematic liquid crystal filled with silica nanoparticles [32].

Thermal properties of nematic liquid crystal colloids can be measured by differential scanning calorimetry (DSC). PMMA (*d*=150 nm, coated with PHSA) were dispersed into 5CB and MBBA, both of which are nematic liquid crystal, respectively [30]. Nematic to isotropic transition temperature decreases with increasing concentration of PMMA nanoparticles as figure 2.25 shows. The shift in the transition temperature T_c is due to the elastic energy around the particles given by

$$T_c(\phi) \sim T_0(1-\frac{\xi^2}{R^2}\phi)\,, \tag{2.7}$$

where T_0 is the transition temperature of pure nematic liquid crystal, R is radius of the particles, and ξ is the nematic correlation length depending on anchoring strength and nematic interaction of liquid crystal [33].

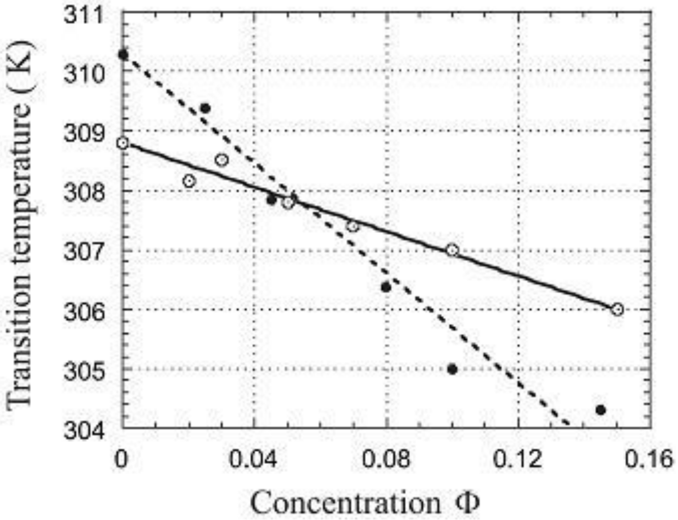

Fig. 2.25 Dependence of nematic to isotropic transition temperature on particle concentration. Solid line is a linear fit for 5CB (hollow circle), and dashed line is linear fit for MBBA (dark circle) [30].

Investigations of mechanical properties were also performed [14, 30]. Figure 2.26 shows storage modules of 5CB dispersed with PMMA (*d*=150 nm, coated with PHSA) nanoparticles, as a function of particle concentration. In this experiment, a Dynamic Stress Rheometer with parallel plate set-up was utilized. A sinusoidal shear stress of low frequency 1 Hz was applied to the sample and the resulting shear strain is measured. The storage modulus is given by

$$G' = \frac{\sigma_0}{\varepsilon_0} \cos\delta \,, \tag{2.8}$$

where σ_0 is stress, ε_0 is consequent strain and δ is the phase lag between stress and strain.

Yield stress, the stress at which the colloids began to deform plastically, was also measured in the same experiment. Dependence of yield stress on particle concentration is shown by figure 2.27.

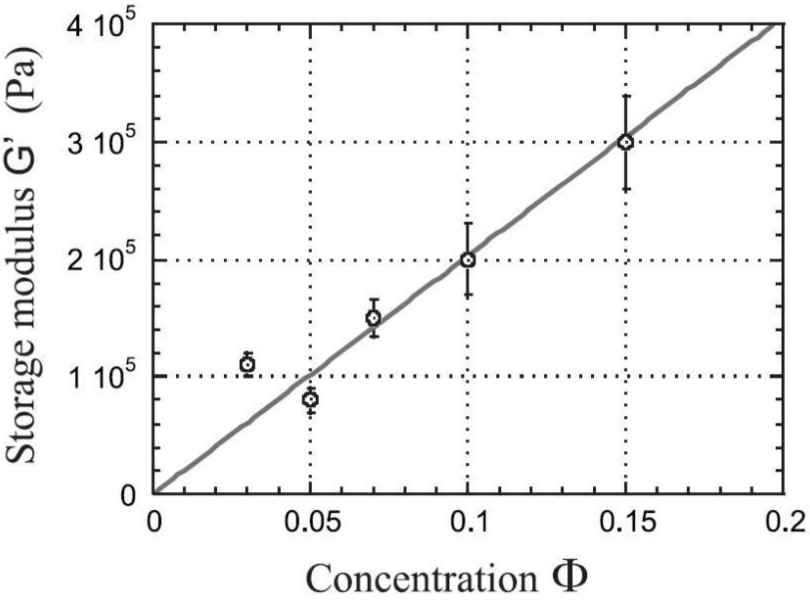

Fig. 2.26 Dependence of storage modulus on the particle concentration at constant frequency 1 Hz at 15 ℃ [30].

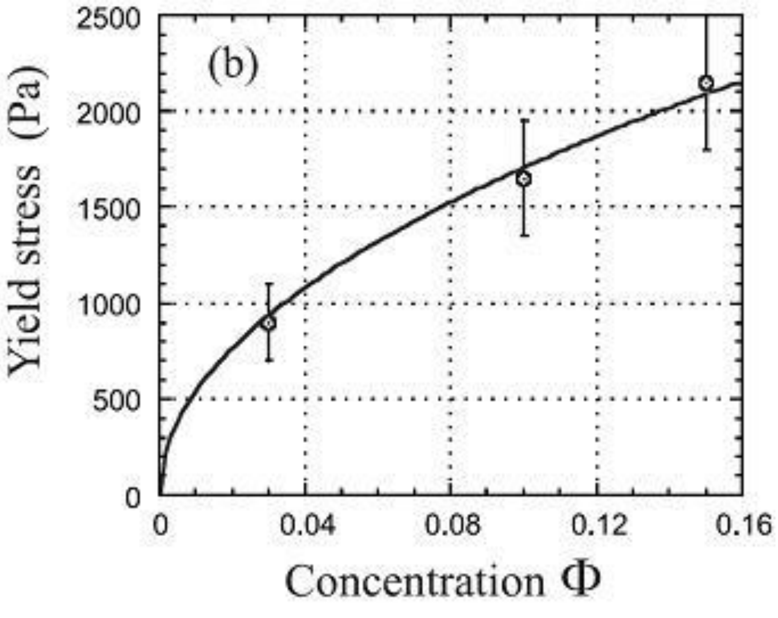

Fig. 2.27 Dependence of yield stress on the particle concentration at constant frequency 1 Hz at 15 ℃ [30].

3 Basics of x-rays and x-ray scattering

X-rays were first discovered by W. Roentgen in 1895. Since their discovery, x-rays have been widely researched and utilized in many aspects, the typical and common ones of which are x-ray crystallography, medical uses and airport security etc.

3.1 Properties and generation of x-rays

3.1.1 Properties of x-rays and x-ray tube

X-rays are electromagnetic waves with wavelength in the range of 0.01 to 10 nm as figure 3.1 shows, corresponding to frequencies in the range of 3×10^{16} to 3×10^{19} Hz. In synchrotron radiation, commonly x-rays with energy lower than 4 keV are classified as soft x-rays while those higher than 4 keV are classified as hard x-rays, due to their penetrating properties.

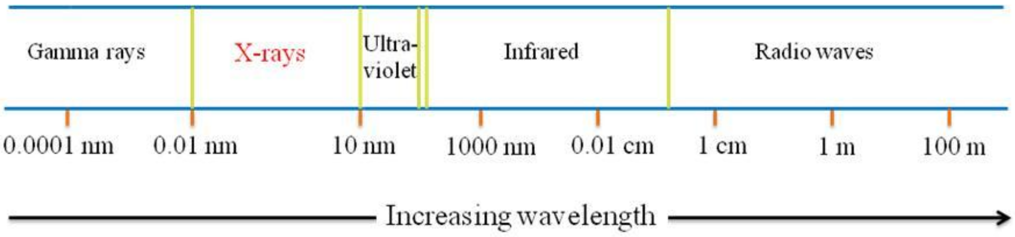

Fig. 3.1 X-rays within the electromagnetic spectrum.

Physically x-rays exhibit a wave-particle duality just like other lights. In the aspect of wave, x-rays are characterized by wavelength λ, frequency v and wave velocity c (the speed of light) as

$$\lambda = \frac{c}{v}. \tag{3.1}$$

When regarded as particles, that is, photons, x-rays are characterized by energy E and momentum p as

$$E = hv$$
$$p = \frac{h}{\lambda}, \tag{3.2}$$

where h is Planck's constant (6.626×10^{-34} Js).

A numerical relationship between photon energy E in the unit keV and wavelength λ in Å can be given as

$$\lambda = \frac{12.4}{E} . \tag{3.3}$$

X-rays are generated mainly by two methods, x-ray tube and synchrotron radiation. Synchrotron radiation will be introduced later in this chapter. Spectrum from synchrotron radiation covers x-ray range. By applying monochromator or mirrors, we can select x-rays with specific wavelength or energy.

The other way to generate x-rays, which is also the traditional way, is using an x-ray tube, which is a vacuum tube with a high voltage to accelerate the electrons released by a hot cathode to a high velocity. The electrons with high velocity collide with the anode, usually a metal target, and create x-rays simultaneously. This process can be interpreted by figure 3.2 [34].

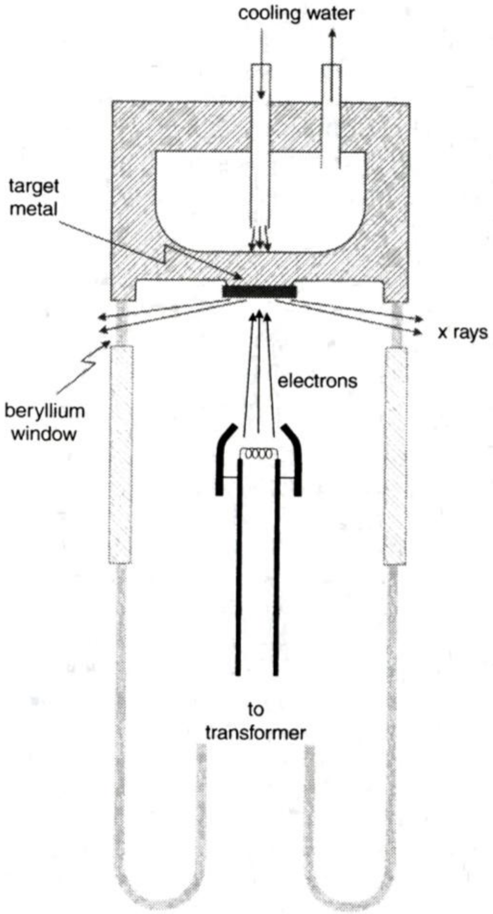

Fig. 3.2 Schematic illustration of a sealed x-ray tube [34].

The maximum energy of the produced x-ray photon is limited by the energy of the incident electrons. K-series spectral lines of target metals are commonly utilized. Typical K-series spectral line wavelengths of some common target metals are shown in table 3.1.

Table 3.1 K-series spectral line wavelengths of typical target metals

Element	Atomic number	K_α / Å	K_β / Å
Cr	24	2.2909	2.08479
Fe	26	1.9373	1.75654
Co	27	1.7902	1.62073
Ni	28	1.6591	1.50008
Cu	29	1.5418	1.39217
Mo	42	0.7107	0.63225

3.1.2 Physics of synchrotron radiation (SR)

Synchrotron radiation is an electromagnetic radiation generated by the acceleration of relativistic charged particles through magnetic fields in a synchrotron. It was first announced in 1947 by Frank Elder [35]. It covers a whole spectrum from radio waves to visible rays, x-rays and gamma rays.

3.1.2.1 Electromagnetic fields from a moving charged particle

The theory of synchrotron radiation is initially related to the electromagnetic fields generated by moving charged particles. It can be derived from Maxwell’s equations that any charged particles under the influence of external forces can emit radiation. For example, as illustrated in figure 3.3 [37], for a moving point charge e, the electric and magnetic fields are given by equation (3.4). For the detailed theoretic derivation, we can refer to references [36, 37].

$$\begin{aligned}\mathbf{E}(t) &= \frac{e}{4\pi\varepsilon_0}\left\{\frac{(1-\beta^2)(\mathbf{n}-\boldsymbol{\beta})}{r^2(1-\mathbf{n}\cdot\boldsymbol{\beta})^3}+\frac{\left[\mathbf{n}\times\left[(\mathbf{n}-\boldsymbol{\beta})\times\dot{\boldsymbol{\beta}}\right]\right]}{cr(1-\mathbf{n}\cdot\boldsymbol{\beta})^3}\right\}, \\ \mathbf{B}(t) &= \frac{\left[\mathbf{n}_{ret}\times\mathbf{E}\right]}{c}\end{aligned} \tag{3.4}$$

where $\mathbf{E}(t)$ is electric field, $\mathbf{B}(t)$ is magnetic field, ε_0 is permittivity of free space, $\boldsymbol{\beta}=\mathbf{v}/c$ is normalized velocity, $\mathbf{n}=\mathbf{r}/r$ is a unit vector, r is the distance between observation point and charge e, $c=3.0\times10^8$ m/s is the speed of light at free space.

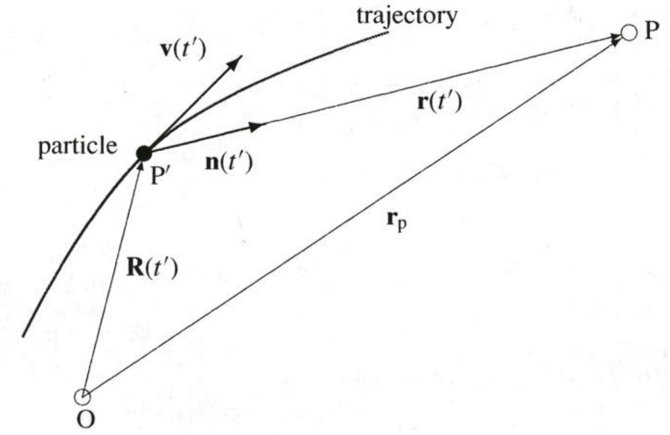

Fig. 3.3 The particle trajectory and radiation geometry [37].

In (3.4), **E**(*t*) has two terms, the first one is inverse proportional to the square of *r*. The second one is inverse proportional to *r*, which means the second term decays much slower than the first term as *r* increases. In actual synchrotron facilities, *r* is quite large that only the second term is taken into account.

In this case, **E**(*t*) can be expressed as equation (3.5), from which we can see **E**(*t*) depends on the velocity **v** as well as on the acceleration of the charge *e*.

$$\mathbf{E}(t) = \frac{e}{4\pi\varepsilon_0}\left\{\frac{\left[\mathbf{n}\times\left[(\mathbf{n}-\boldsymbol{\beta})\times\dot{\boldsymbol{\beta}}\right]\right]}{cr(1-\mathbf{n}\cdot\boldsymbol{\beta})^3}\right\}. \tag{3.5}$$

For synchrotron radiation, the electrons are moving at a speed near *c*. The resultant **β**=**v**/*c* is approximately equal to 1. From (3.5), it can be seen that along the direction of **v**, the term 1-**n v** is approximately equal to 0, resulting in a very large *E*(*t*).

3.1.2.2 Synchrotron radiation facility

From theoretical description it can be seen that synchrotron radiation can be produced by accelerating moving charged particles, and actually, synchrotron radiation is produced from accelerators which are called storage rings.

A typical synchrotron radiation facility is composed of electron gun which generates electrons, linear accelerator which accelerates electrons preliminarily, booster ring which further accelerates the electrons to a speed near the speed of light, storage ring which accepts electrons from booster ring and circulate the electrons to generate radiation and finally experimental station which uses generated synchrotron radiation to perform experiments. The main storage ring components are illustrated by figure 3.4 [36].

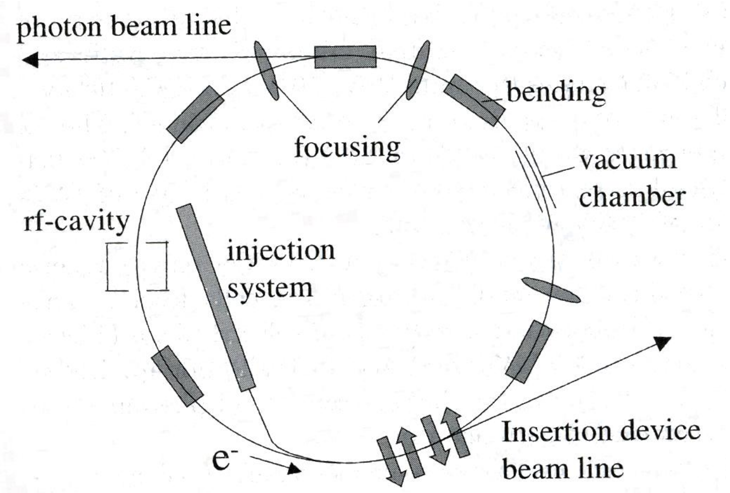

Fig. 3.4 General storage ring components [36].

In order to generate radiation from storage rings, the charged particles must be accelerated to circulate. This is usually achieved by introducing magnetic field, including bending magnets and insertion devices. Insertion devices are periodical magnetic devices such as wiggler or undulator.

3.1.2.3 Properties of SR

Synchrotron radiation has some distinct properties as will be briefly summarized here. All the properties introduced here can be theoretically calculated by applying classical electrodynamics to moving relativistic charged particles. For detailed illustration, we can refer to references [34, 36-37].

High brilliance:

Brilliance is defined as

$$Brilliance = \frac{Photons/\text{second}}{(mrad)^2\ (mm^2\ source\ area)(0.1\%\ bandwidth)},$$

where *mrad* is the unit for solid angle.

The maximum brilliance from the third generation synchrotron radiation facility, which introduces insertion devices, is more than 10 orders of magnitude higher than that from a rotating anode. This dramatic improvement has in many ways led to a remarkable shift in experimental x-ray science.

Continuous broad spectrum:

Spectrum of synchrotron radiation is very broad and continuous, ranging from the infrared ($\lambda \sim 10^{-2}$ cm) to the hard x-rays ($\lambda \sim 10^{-2}$ nm). The spectrum depends on the energy E of the electron beam circulating in the storage ring and the radius of curvature R of its trajectory. For radiation from bending magnets, λ is proportional to R/E^3.

High degree polarization:

For x-rays emitted in the plane of the electron orbit, the radiation is completely linearly polarized, with the electric vector of the radiation parallel to the plane of orbit. For the x-rays emerging in the direction not exactly on the orbital plane, the radiation is elliptically polarized, with a small vertically polarized component present.

Small angular divergence:

At relativistic speed, the electrons forced in the storage ring emit radiation which is sharply concentrated along the same direction of their motion. Angular divergence of the radiation in the direction perpendicular to the plane of the electron orbit is very small as figure 3.5 shows. The vertical divergence $\Delta\psi$ is of the order mc^2/E which can be estimated to be only a fraction of a milliradian when the electron energy is in the order of GeV.

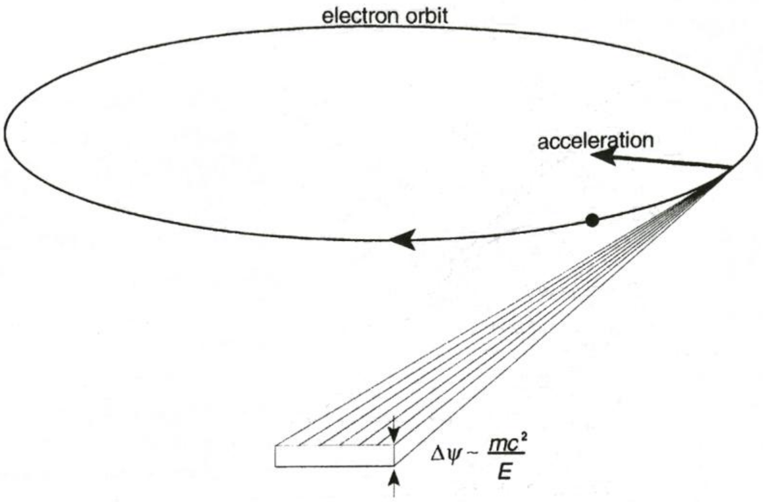

Fig. 3.5 Angular distribution of synchrotron radiation [34].

Based on those properties and advantages compared to conventional x-rays generated by x-ray tubes, synchrotron radiation has been put into wide use in a variety of disciplines such as surface science, material science, environmental science and biological science etc.

3.2 Scattering of x-rays

In classical description of the scattering event, the electric field of the incident x-ray exerts a force on the electronic charge, which then accelerates and radiates the scattered wave. Here in this section, the theory concerning x-ray scattering will be introduced.

3.2.1 Electromagnetic field radiated from a charged distribution

Maxwell's equations can be compiled into [38]

$$\mathbf{E} = -\nabla\phi - \frac{\partial \mathbf{A}}{\partial t}, \tag{3.6}$$

$$\mathbf{B} = \nabla \times \mathbf{A}, \tag{3.7}$$

where **E** is the electric field, **B** is the magnetic field, φ is the electric potential (scalar potential). **A** is the magnetic vector potential defined by equation (3.7).

By solving the wave equations, it can be shown that

$$|\mathbf{E}| = c|\mathbf{B}|. \tag{3.8}$$

Based on these three equations, if we know **A**, then **B** and **E** can be deduced consequently.

A is described by the equation

$$\mathbf{A}(\mathbf{r},t) = \frac{1}{4\pi\varepsilon_0 c^2}\int_v \frac{\mathbf{J}(\mathbf{r}',t-|\mathbf{r}-\mathbf{r}'|/c)}{|\mathbf{r}-\mathbf{r}'|}d\mathbf{r}', \tag{3.9}$$

where **J**(**r'**,*t*) is the current density of the source as shown in figure 3.6 [35]. The fields observed at point ***X*** at time *t* depend on the position of the electron at an earlier time *t*-|**r**-**r'**|/*c*. For detailed derivation, we can refer to reference [38], here only the final calculated electromagnetic field is given

$$\mathbf{B} \approx \left(\frac{1}{4\pi\varepsilon_0 c^2}\right)\frac{1}{cr}\ddot{\mathbf{p}}(t')\times\hat{\mathbf{r}}, \tag{3.10}$$

$$\mathbf{E}(t) = \left(\frac{1}{4\pi\varepsilon_0 c^2}\right)\frac{1}{r}\left[\hat{\mathbf{r}} \times \left(\hat{\mathbf{r}} \times \ddot{\mathbf{p}}(t')\right)\right], \tag{3.11}$$

where **p** is electric dipole moment as figure 3.7 [35] shows.

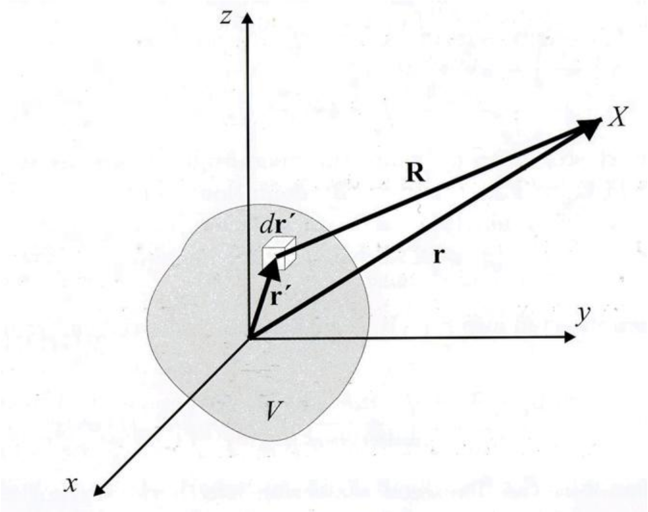

Fig. 3.6 Coordinate system to calculate the electromagnetic field radiated from a charge distribution [35].

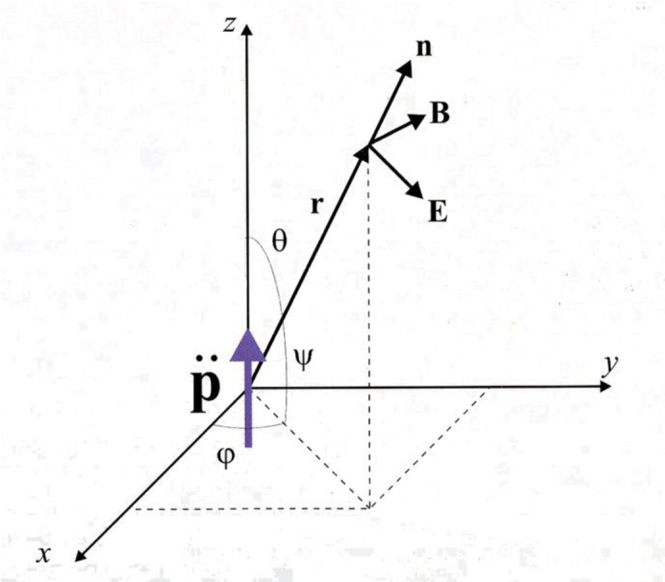

Fig. 3.7 An electromagnetic plane wave polarized with its electric field along the *z* axis forces an electric dipole at the origin to oscillate [35].

3.2.2 Scattering from an electron

Before intruding scattering from an electron, the concepts of flux should be given in advance [34]. Flux is to describe the strength of radiation. In the case of wave, flux density J is proportional to the square of the amplitude A of the oscillating wave field. With the amplitude expressed as a complex number, J is given by

$$J = |A|^2 = AA^*, \tag{3.12}$$

where A^* is the complex conjugate of A.

As shown in figure 3.8 [34], a free electron placed at position O is irradiated with a beam of x-rays of flux J_0 propagating in X-direction. The detector is placed at point P in the XY plane at a large distance R from O. The scattering angle between OX and OP is 2θ. Electric field vector E_0 is in YZ plane perpendicular to propagation direction X.

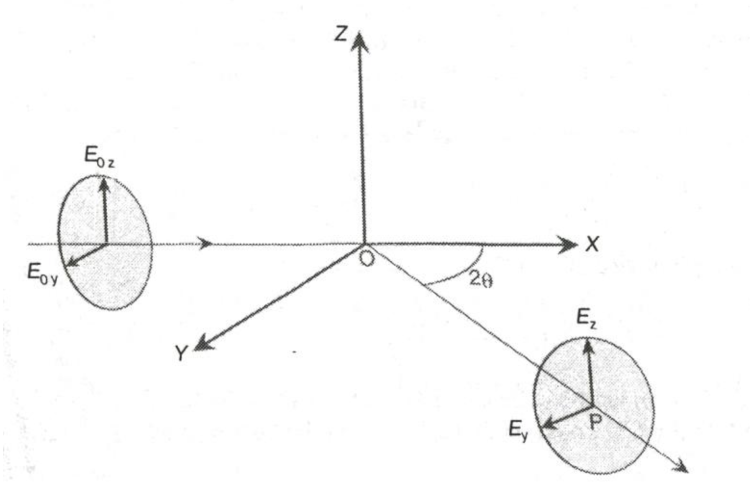

Fig. 3.8 Scattering of an unpolarized x-ray by a single free electron at the origin [34].

If an incident beam is polarized in the Z direction, with the magnitude of its electric field vector E_{0z}. According to (3.11), the free electron at O will oscillate in the Z direction and induce emission of an electromagnetic radiation of the same frequency propagating in all directions. At P

$$E_z = E_{0z} \frac{1}{4\pi\varepsilon_0} \frac{e^2}{mc^2} \frac{1}{R}. \tag{3.13}$$

If an incident beam is polarized in the Y direction, with the magnitude of its electric field vector E_{0y}. At P

$$E_y = E_{0y} \frac{1}{4\pi\varepsilon_0} \frac{e^2}{mc^2} \frac{\cos 2\theta}{R} . \tag{3.14}$$

For an unpolarized x-ray beam with the magnitude of its electric field vector E_0, the time averages of E^2_{0y} and E^2_{0z} obey

$$E_0^2 = \left\langle E_{0y}^2 \right\rangle + \left\langle E_{0z}^2 \right\rangle, \left\langle E_{0y}^2 \right\rangle = \left\langle E_{0z}^2 \right\rangle = \frac{1}{2} E_0^2 . \tag{3.15}$$

The flux of energy reaching a unit area per second at P is given by

$$E^2 = \left\langle E_y^2 \right\rangle + \left\langle E_z^2 \right\rangle = J_0 (\frac{1}{4\pi\varepsilon_0})^2 (\frac{e^2}{mc^2})^2 \frac{1}{R^2} \frac{1+\cos^2 2\theta}{2} , \tag{3.16}$$

where $J_0=E^2_0$.

This unit area at P contains a solid angle$1/R^2$, therefore the energy scattered in OP direction per unit angle per second, which is the flux J_e of the scattered x-ray is

$$J_e = J_0 (\frac{1}{4\pi\varepsilon_0})^2 (\frac{e^2}{mc^2})^2 \frac{1+\cos^2 2\theta}{2} . \tag{3.17}$$

(3.17) is called the Thomson formula for the scattering of x-rays by a single electron.

Classical radius of the electron r_e is defined as

$$r_e = \frac{1}{4\pi\varepsilon_0} \frac{e^2}{mc^2} . \tag{3.18}$$

r_e has a dimension of length with the value 2.818 $\times 10^{-15}$ m.

The scattering length of an electron for unpolarized x-ray is given by (3.19)

$$b_e = \frac{E}{E_0} = \sqrt{\frac{J}{J_0}} = r_e \left(\frac{1+\cos^2 2\theta}{2} \right)^{1/2} . \tag{3.19}$$

It should be noted that this form is valid only when the incident beam is unpolarized.

3.2.3 Scattering from an atom

X-rays scattered from different electrons will interfere with each other, resulting in a constructive or destructive interference. The amplitude of x-rays scattered from N electrons at positions **r**$\mathbf{r}_\mathbf{j}$(j=1…N) is given by

$$A(q) = A_0 b_e \sum_{j=1}^{N} e^{-i2\pi\, q\cdot r_j} \;, \tag{3.20}$$

where A_0 is the amplitude of incident x-ray, **q** is scattering vector which is the vector difference between the wave propagation vectors of the incident and the scattered beam, both of length $2\pi/\lambda$, where λ is the wavelength of the scattered radiation in the medium. The magnitude of **s** can be expressed as

$$|\mathbf{q}| = \frac{4\pi \sin\theta}{\lambda} \,. \tag{3.21}$$

Within an atom, the electrons can be expressed by electron density distribution $n(r)$. In this way, the amplitude of x-ray scattered from an atom, measured in unit of $A_0 b_e$, is called the atomic scattering factor as

$$f(q) = \int n(r) e^{-i2\pi\, q\cdot r} dr \,. \tag{3.22}$$

Using spherical polar coordinate system, (3.22) can be rewritten to

$$f(q) = \int_0^\infty 4\pi r^2 n(r) \frac{\sin 2\pi q r}{2\pi q r} dr \,. \tag{3.23}$$

3.2.4 Scattering from a whole sample

Sample can be considered to be an assembly of different atoms. With this consideration, the position vector $\boldsymbol{r}_j$ of an electron can be written as

$$r_j = r_k + r_{k,m} \,, \tag{3.24}$$

where $\boldsymbol{r}_k$ is the position of the center of the kth atom (k=1…N_{atom}), and $\boldsymbol{r}_{k,m}$ is the position of the electron (m=1…Z) within the kth atom from its center.

Equation (3.19) becomes

$$A(q) = A_0 b_e \sum_{k=1}^{N_{atom}} \left(\sum_{m=1}^{Z} e^{-i2\pi\, q\cdot r_{k,m}} \right) e^{-i2\pi\, q\cdot r_k} \,, \tag{3.25}$$

$$A(q) = A_0 b_e \sum_{k=1}^{N_{atom}} f_k(q) e^{-i2\pi\, q\cdot r_k} \,, \tag{3.26}$$

where $f_k(q)$ is the atomic scattering factor of the kth atom.

Here a parameter called scattering length density distribution $\rho(\mathbf{r})$ is introduced to substitute the electron density $n(\mathbf{r})$ and the relation between these two parameters is given by

$$\rho(\mathbf{r}) = b_e \cdot n(\mathbf{r})\,. \tag{3.27}$$

In general, the relationship among several most important physical parameters can be summarized as following figure 3.9. $\rho(\mathbf{r})$ is scattering length density distribution in real space $\mathbf{r}$, $\Gamma_\rho(\mathbf{r})$ is autocorrelation function of $\rho(\mathbf{r})$, $A(\mathbf{q})$ is scattering wave in reciprocal space $\mathbf{q}$ and $I(\mathbf{q})$ is scattering intensity at $\mathbf{q}$.

$$\begin{tikzcd}
\rho(r) \arrow[r, shift left, "\text{Fourier transform}"] \arrow[d, "\text{autocorrelation}"'] & A(q) \arrow[l, shift left, "\text{inverse Fourier transform}"] \arrow[d, "\text{squaring}"] \\
\Gamma_\rho(r) \arrow[r, shift left, "\text{Fourier transform}"] & I(q) \arrow[l, shift left, "\text{inverse Fourier transform}"]
\end{tikzcd}$$

Fig. 3.9 Relationship among $\rho(\mathbf{r})$, $\Gamma_\rho(\mathbf{r})$, $A(\mathbf{q})$ and $I(\mathbf{q})$ [34].

By introducing $\rho(\mathbf{r})$ and $\Gamma_\rho(\mathbf{r})$, the scattered intensity can be expressed as

$$I(\mathbf{q}) = \left|A(\mathbf{q})\right|^2 = \left|\int_V \rho(\mathbf{r}) e^{-i\mathbf{qr}} d\mathbf{r}\right|^2 . \tag{3.28}$$

$I(\mathbf{q})$ can be expressed as

$$\begin{aligned} I(\mathbf{q}) &= A(\mathbf{q}) \cdot A^*(\mathbf{q}) \\ &= \left[\int_V \rho(\mathbf{u'}) e^{-i\mathbf{qu'}} d\mathbf{u'}\right]\left[\int_V \rho(\mathbf{u}) e^{-i\mathbf{qu}} d\mathbf{u}\right]. \\ &= \int \Gamma_\rho(\mathbf{r}) e^{-i\mathbf{qr}} d\mathbf{r} \end{aligned} \tag{3.29}$$

Let us denote the mean value of $\rho(\mathbf{r})$ throughout the sample by $<\rho>$ and the deviation of $\rho(\mathbf{r})$ from its mean by

$$\eta(\mathbf{r}) = \rho(\mathbf{r}) - <\rho>. \tag{3.30}$$

It can de derived that

$$\Gamma_\rho(\mathbf{r}) = \Gamma_\eta(\mathbf{r}) + <\rho>^2 V\,, \tag{3.31}$$

where V is the volume of the sample.

Finally, scattering intensity from a whole sample can be given as

$$I(\mathbf{q}) = \int \Gamma_\eta(\mathbf{r}) e^{-i\mathbf{qr}} d\mathbf{r} + <\rho>^2 V\delta(\mathbf{q})\,. \tag{3.32}$$

The second term of (3.32) cannot be experimentally observed because at **q**=0, the scattered signal is strongly influenced by the much stronger transmitted direct beam.

(3.32) indicates that the strength and pattern of scattering from a sample is not determined by the absolute value of the scattering length density but the difference of the scattering length density in the sample. To increase the scattered intensity from a sample, we have to increase the contrast in the scattering length density among different atoms or regions within the sample.

3.3 Small angle x-ray scattering (SAXS)

Small angle x-ray scattering, usually abbreviated as SAXS, is an x-ray scattering method when scattering angle is small.

3.3.1 Principles of SAXS

A typical x-ray scattering can be generally schemed as figure 3.10. 2θ is defined as scattering angle. When 2θ<10°, it's often defined as SAXS. The formula and principles introduced previously on x-ray scattering can be utilized in SAXS.

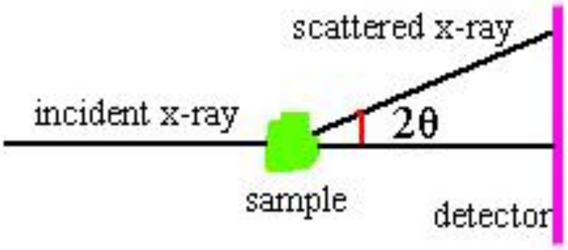

Fig. 3.10 A typical x-ray scattering experimental setup.

As previously introduced, the magnitude of **q** can be expressed as

$$|\mathbf{q}| = \frac{4\pi \sin\theta}{\lambda}\,, \tag{3.33}$$

where θ is half the scattering angle as shown in figure 3.10.

The reciprocity between real space and reciprocal space means that information on relatively large scales in real space is contained at relatively small **q**. On the contrary, small **q** corresponds to a larger structure in real space. SAXS is a fundamental method for determination of the microscale or nanoscale structures of particle systems. Besides, it can also detect the structures of ordered systems like lamellae and fractal materials.

3.3.2 Application of SAXS

SAXS can reveal information of shapes, averaged particle sizes, interparticle structure and surface area of the samples. It is widely utilized to study colloids, metals, polymers, plastics, foods and proteins.

3.3.2.1 Shape of simple geometric particles

The application of SAXS to investigate the shapes is based on the fact that scattering intensity from particles of simple geometric shape has instinctive characteristics which are determined by the shape of the particles. Here we briefly introduce the scattering intensity from sphere, thin rod and thin circular disk. For detailed derivation, we can refer to [34].

Scattering intensity from a sphere is given by

$$I(q) = \rho_0^2 v^2 \frac{9(\sin qR - qR\cos qR)^2}{(qR)^6}, \tag{3.34}$$

where v is the volume of the sphere, ρ_0 is the uniform density within the radius R.

Scattering intensity from a thin rod is given by

$$I(q) = \rho^2 v^2 \frac{2}{qL}[Si(qL) - \frac{1-\cos qL}{qL}], \tag{3.35}$$

where L is the length of the rod.

$Si(x)$ is the sine integral function defined as

$$S_i(x) = \int_0^x \frac{\sin u}{u} du\,. \tag{3.36}$$

Scattering intensity from a thin circular disk is given by

$$I(q) = \rho_0^2 v^2 \frac{2}{q^2R^2}[1 - \frac{J_1(2qR)}{qR}], \tag{3.37}$$

where $J_1(x)$ is the first-order Bessel function.

We can plot the scattering intensity from spheres, thin disks and thin rods together as figure 3.11 shows [34].

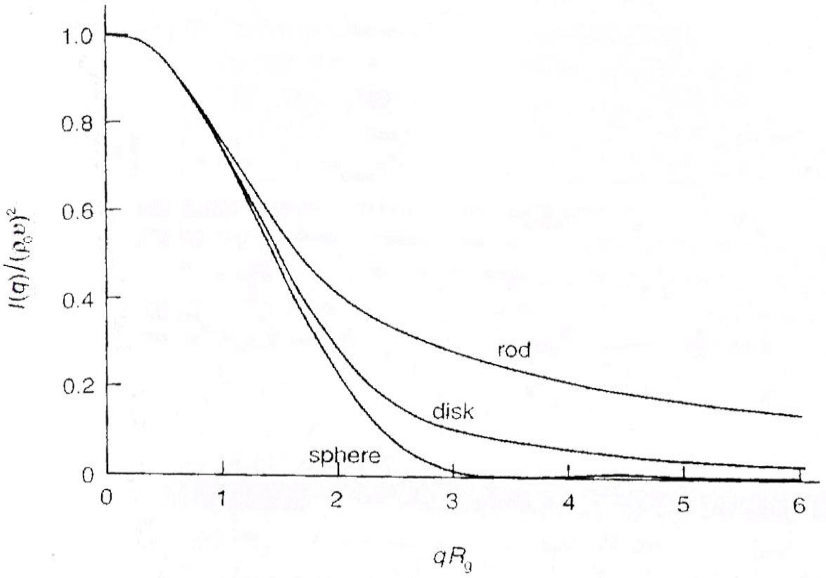

Fig. 3.11 Plot of independent scattering intensities from spheres, thin disks and thin rods [34].

The asymptotic form of intensity curves at an appropriate range can be represented by

$$I(q) \sim q^{-\alpha}\ . \tag{3.38}$$

α is equal to 4 for spheres, 2 for thin disks and 1 for thin rods.

3.3.2.2 Size of particles

Determination of the average size of particles in the sample is based on Guinier law. That is no matter what shape the particle is, the scattering intensity follows a certain universal form, in the limit of small **q**, $I(\mathbf{q})$ can be given by

$$I(q) = \rho_0^2 v^2 \exp(-\frac{1}{3} q^2 R_g^2)\ , \tag{3.39}$$

where R_g is the radius of gyration of a particle of unknown shape and size. Special attention should be paid that Guinier law is valid provided that q is much smaller than $1/R_g$ and that the system is dilute and isotropic.

3.3.2.3 Interparticle structure

For systems where interparticle interactions can not be neglected, $I(q)$ has to take account of interaction among the particles. In this case, $I(q)$ can be written as

$$I(q) \propto F(q)S(q), \tag{3.40}$$

where $F(q)$ is form factor determined by the shape and size of the particles such as equation (3.34) in the case of spherical particle. $S(q)$ is structure factor which reveals the arrangement of particles or the interparticle structures of the particles.

3.3.2.4 Surface area

This application is based on Porod law. For the ideal two-phase system, as $q \rightarrow \infty$, $I(q)$ can be given by

$$I(q) \propto \frac{2\pi(\Delta\rho)^2 S}{q^4}, \tag{3.41}$$

where S is total area of the boundaries between the two phases in the scattering volume.

3.4 Microbeam wide angle x-ray scattering (Microbeam WAXS)

Wide angle x-ray scattering (WAXS) is a method to investigate the crystalline structure of materials by analyzing Bragg Peaks scattered to wide angles. WAXS is a technique similar to SAXS but the diffraction maxima at larger angles are observed.

Microbeam WAXS is a specific experimental method of WAXS with the incident beam size constricted to several microns. This can be achieved nowadays thanks to the development of high brilliant x-ray sources and focusing optics. Microbeam WAXS is to reveal the information of local areas and by scanning the sample, the spatial inhomogeneity can be studied. By combining microbeam WAXS and microbeam SAXS, polymer crystallization, spatial inhomogeneity analyses, stress transfer under external field and the microphase separated structure analyses in block copolymer systems can be investigated [39].

3.5 X-ray photon correlation spectroscopy (XPCS)

X-ray photon correlation spectroscopy (XPCS) is the x-ray analog of dynamic light scattering (DLS) and is a relatively new technique which uses coherent x-ray beams to study dynamic phenomena. XPCS is a useful complementary method to many other methods especially in detecting the low frequency dynamics as figure 3.12 shows [40]. XPCS can study the dynamics of samples on time scales from seconds down to microseconds and length scales from microns to nanometers.

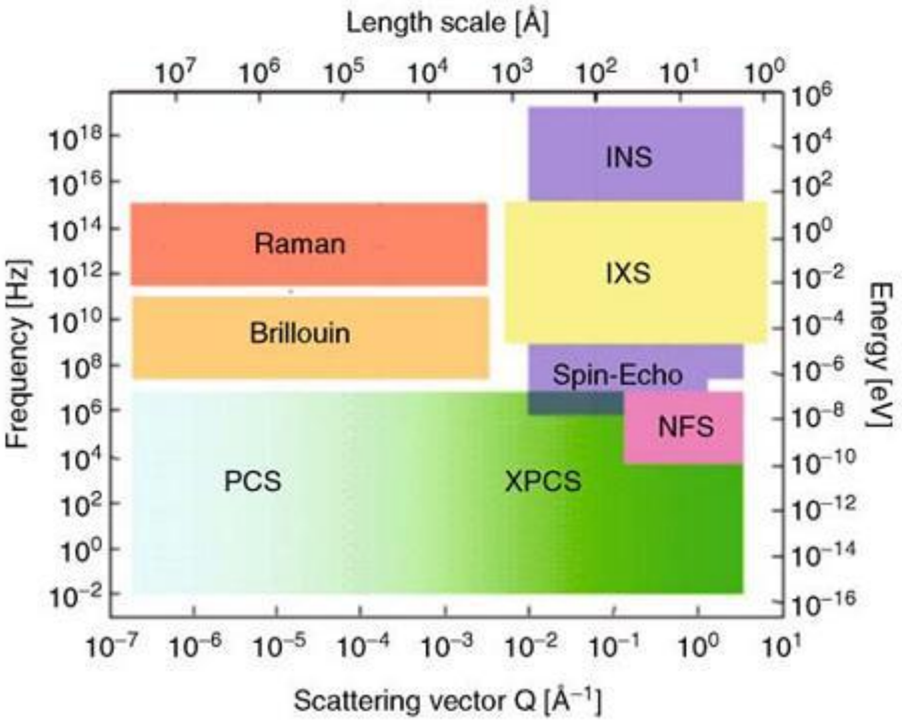

Fig. 3.12 Frequency-scattering vector space covered by XPCS and some other complementary techniques [40].

3.5.1 Principles of XPCS

Form the background of x-ray scattering as introduced in the previous sections, we know that scattering intensity is determined by the electron density distribution $n(r)$ or the scattering length density distribution $\rho(r)$ of the sample. In the case the sample is composed of particles, $\rho(r)$ will fluctuate as the particles fluctuate, resulting in the fluctuation of scattering intensity. On the contrary, by analyzing the fluctuation of scattering intensity, we can reveal some information of the fluctuation of the particles, or the dynamics of the particles. This is the general principle of XPCS.

Experimentally, if coherent light is scattered from a disordered system, it generates a random scattering or “speckle” pattern. If the spatial arrangement of the disordered system changes with time, the corresponding speckle pattern will also change and the intensity fluctuation of the speckles can provide information on the underlying dynamics. XPCS probes the dynamic properties of matter by analyzing the temporal correlations among photons scattered by the studied material.

3.5.1.1 Normalized intensity autocorrelation function

The quantity measured in XPCS measurements is the normalized intensity autocorrelation function, defined as [40]

$$g_2(q,t) = \frac{< I(\mathbf{q},t')I(\mathbf{q},t'+t) >}{< I(\mathbf{q},t') >^2}, \tag{3.42}$$

where $< I(\mathbf{q},t')I(\mathbf{q},t'+t) >$ is the intensity autocorrelation function, expressed as

$$< I(\mathbf{q},t')I(\mathbf{q},t'+t) >= \lim_{T\to\infty}\frac{1}{T}\int_{t_0}^{t_0+T} I(\mathbf{q},t')I(\mathbf{q},t'+t)dt', \tag{3.43}$$

where **q** is the scattering vector, $I(\mathbf{q},t')$ is the intensity at **q** at time *t’*.

$< I(\mathbf{q},t') >$ is the expected value of $I(\mathbf{q},t')$ during $t_0 \leqq t' \leqq t_0+T$, expressed as

$$< I(\mathbf{q},t') >= \lim_{T\to\infty}\frac{1}{T}\int_{t_0}^{t_0+T} I(\mathbf{q},t')dt'. \tag{3.44}$$

In (3.43), when t=0, $< I(\mathbf{q},t')I(\mathbf{q},t'+t) >$ reaches the maximum as

$$< I(\mathbf{q},t')I(\mathbf{q},t'+t) >=< I(\mathbf{q},t')^2 >. \tag{3.45}$$

When t is large enough, there’s no correlation between $I(\mathbf{q},t')$ and $I(\mathbf{q},t'+t)$

$$< I(\mathbf{q},t')I(\mathbf{q},t'+t) >=< I(\mathbf{q},t') >< I(\mathbf{q},t'+t) >=< I(\mathbf{q},t') >^2. \tag{3.46}$$

During the XPCS data analysis, a discrete form for equation (3.43), (3.44) are introduced as

$$< I(\mathbf{q},t')I(\mathbf{q},t'+t) >= \lim_{N\to\infty}\frac{1}{N}\sum_{j=1}^{N} I(\mathbf{q},j)I(\mathbf{q},j+n)\,, \qquad (3.47)$$

$$< I(\mathbf{q},t') >= \lim_{N\to\infty}\frac{1}{N}\sum_{j=1}^{N} I(\mathbf{q},j)\,, \qquad (3.48)$$

where $t=n\times\Delta t$, $t'=j\times\Delta t$, and Δt is the time interval between each successive frames.

3.5.1.2 Time dependence of normalized intensity autocorrelation function

Single exponential decay:

In many applications, the autocorrelation function decays from $< I(\mathbf{q},t')^2 >$ to $< I(\mathbf{q},t') >^2$ like a single exponential, in this case, $< I(\mathbf{q},t')I(\mathbf{q},t'+t) >$ can be fitted as

$$< I(\mathbf{q},t')I(\mathbf{q},t'+t) >=< I(\mathbf{q},t') >^2 + [< I(\mathbf{q},t')^2 > - < I(\mathbf{q},t') >^2]\exp(\frac{-t}{\tau}), \quad (3.49)$$

where τ is called relaxation time.

For simplicity, the last term of (3.49) can be written as

$$C(t) = [< I(\mathbf{q},t')^2 > - < I(\mathbf{q},t') >^2]\exp(\frac{-t}{\tau}) = a\exp(\frac{-t}{\tau})\,, \qquad (3.50)$$

where a is an amplitude.

Some typical modes of relaxation can be briefly summarized here [40].

Gaussian:

$$C(t) = a\exp\left(\frac{-t^2}{\tau^2}\right). \qquad (3.51)$$

It is commonly used for the study of molecules in a perfect gas, or any particles undergoing perfect-gas-like motion with an equilibrium distribution of velocities.

Sum of exponentials:

$$C(t) = \sum a_i \exp\left(\frac{-t}{\tau_i}\right). \qquad (3.52)$$

This form often occurs when there is more than one independent relaxation process contributing to the correlation function.

Oscillating decay:

$$C(t) = a\cos(\omega t)\exp\left(\frac{-t}{\tau}\right). \tag{3.53}$$

This decay is often measured in scattering from systems when external field imposes a constant velocity on a particle undergoing thermal motion.

Stretched exponential:

$$C(t) = a\exp\left[-\left(\frac{t}{\tau}\right)^{\alpha}\right], \tag{3.54}$$

where the exponent α is smaller than 1. This behavior means that the relaxation process is stretched and a longer relaxation time is expected, indicating a slower dynamics compared to a single exponential behavior.

Compressed exponential:

$$C(t) = a\exp\left[-\left(\frac{t}{\tau}\right)^{\alpha}\right], \tag{3.55}$$

where the exponent α is larger than 1. This behavior means that the relaxation process is compressed and a shorter relaxation time is expected, indicating a faster dynamics compared to a single exponential behavior.

The expression for stretched and compressed exponential is very similar except that the range of exponent α is different. The last two types of correlation function are often used to fit scattering on soft matter systems. The detailed data analysis process can be found from reference [41].

3.5.1.3 Siegert relation

Similar to normalized intensity autocorrelation function, the normalized electric field autocorrelation function is defined as [40]

$$g_1(q,t) = \frac{< E(\mathbf{q},t')E^*(\mathbf{q},t'+t) >}{< E(\mathbf{q},t')E^*(\mathbf{q},t') >}. \tag{3.56}$$

$g_1(q,t)$ is also called normalized intermediate scattering function.

Siegert relation is to describe the relation between $g_1(q,t)$ and $g_2(q,t)$, which is given by

$$g_2(q,t) = 1 + [g_1(q,t)]^2. \tag{3.57}$$

Siegert relation reveals that the fluctuation of particles will generate the fluctuation of electric field scattered by particles, which will subsequently cause the fluctuation of scattering intensity.

Generally the Siegert relation is given by

$$g_2(q,t) = 1 + \beta[g_1(q,t)]^2 , \tag{3.58}$$

where β is the coherence factor, depending on the beam and instrumentation optics. Under fully coherent condition, β=1, while under the fully incoherent condition, β=0.

Here the derivation of Siegert relation will be briefly introduced [75]. XPCS deals with normalized autocorrelation functions, so here we omit pre-factors of electric field and write

$$E(\mathbf{q},t) = \sum_{j=1}^{N} \exp[-i\mathbf{q}\cdot\mathbf{r}_j(t)] . \tag{3.59}$$

Electric field autocorrelation function can be written as

$$\begin{aligned} < E(\mathbf{q},0)E^*(\mathbf{q},t) > &= < \sum_{j=1}^{N}\sum_{k=1}^{N} \exp\{-i\mathbf{q}\cdot[\mathbf{r}_j(0)-\mathbf{r}_k(t)]\} > \\ &= < \sum_{j} \exp\{-i\mathbf{q}\cdot[\mathbf{r}_j(0)-\mathbf{r}_j(t)]\} > \\ &= N < \exp\{-i\mathbf{q}\cdot[\mathbf{r}(0)-\mathbf{r}(t)]\} > . \end{aligned} \tag{3.60}$$

$g_1(q,t)$ can be written as

$$g_1(q,t) = \frac{< E(\mathbf{q},0)E^*(\mathbf{q},0+t) >}{< E(\mathbf{q},0)E^*(\mathbf{q},0) >} = < \exp\{-i\mathbf{q}\cdot[\mathbf{r}(0)-\mathbf{r}(t)]\} > . \tag{3.61}$$

Intensity autocorrelation function can be written as

$$\begin{aligned} &< I(\mathbf{q},0)I(\mathbf{q},t) > \\ &= < \sum_{j=1}^{N}\sum_{k=1}^{N} \exp\{-i\mathbf{q}\cdot[\mathbf{r}_j(0)-\mathbf{r}_k(0)]\} \sum_{l=1}^{N}\sum_{m=1}^{N} \exp\{-i\mathbf{q}\cdot[\mathbf{r}_l(t)-\mathbf{r}_m(t)]\} > \\ &= \sum_{j}\sum_{k}\sum_{l}\sum_{m} < \exp\{-i\mathbf{q}\cdot[\mathbf{r}_j(0)-\mathbf{r}_k(0)+\mathbf{r}_l(t)-\mathbf{r}_m(t)]\} > \\ &= \sum_{j}1\sum_{l}1 + \sum_{j} < \exp\{-i\mathbf{q}\cdot[\mathbf{r}_j(0)-\mathbf{r}_j(t)]\} > \sum_{k} < \exp\{-i\mathbf{q}\cdot[\mathbf{r}_k(0)-\mathbf{r}_k(t)]\} > \\ &= N^2 + N^2 < \exp\{-i\mathbf{q}\cdot[\mathbf{r}(0)-\mathbf{r}(t)]\} >^2 . \end{aligned}$$

$g_2(q,t)$ can be written as

$$g_2(q,t) = \frac{< I(\mathbf{q},0) I(\mathbf{q},0+t) >}{< I(\mathbf{q}) >^2} = 1 + < \exp\{-i\mathbf{q} \cdot [\mathbf{r}(0) - \mathbf{r}(t)]\} >^2 \\ = 1 + [g_1(q,t)]^2 \ . \tag{3.62}$$

3.5.2 Experimental requirement

To perform XPCS experiments, coherent or partially coherent x-rays are necessary. As equation (3.58) shows, under fully incoherent condition, $g_2(q,t)$ will be constantly equal to 1, thus no dynamics can be approached.

To interpret coherence, the longitudinal coherence length and transverse coherence length are referred to. Derivation of longitudinal and transverse coherence length can be derived from figure 3.13 and 3.14 [38].

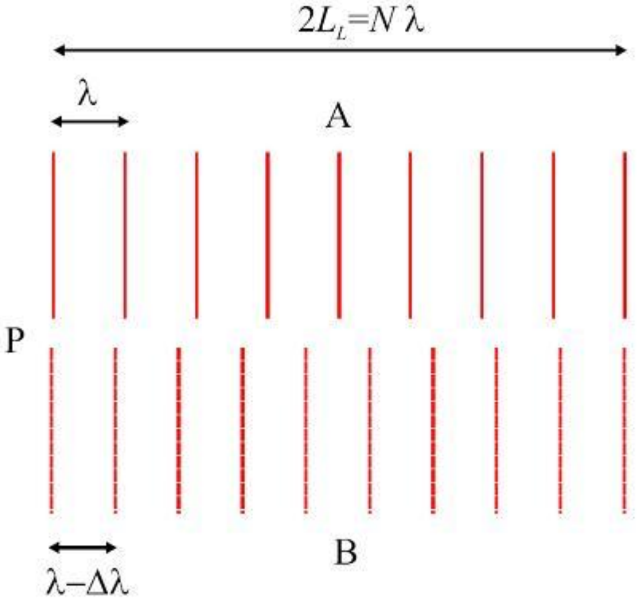

Fig. 3.13 Derivation of longitudinal coherence length L_L [38].

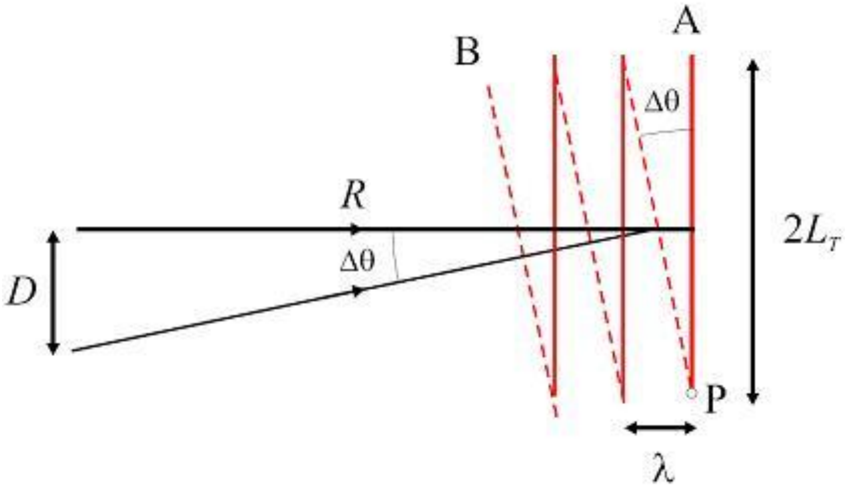

Fig. 3.14 Derivation of transverse coherence length L_T [38].

In figure 3.12, two waves A with wavelength λ and B with wavelength λ-$\Delta\lambda$ are propagating in exactly the same direction. They are exactly in phase at point P. Longitudinal coherence length L_L is to indicate the length from P out of which the two waves will be out of phase. The two waves will be out of phase at L_L and will be exactly in phase again at 2L_L. Let the distance be N wavelengths λ, or equivalently (N+1)(λ-$\Delta\lambda$)

$$\begin{aligned} 2L_L &= N\lambda = (N+1)(\lambda - \Delta\lambda) \\ &= N\lambda + \lambda - (N+1)\Delta\lambda \end{aligned} . \tag{3.63}$$

We can obtain

$$\lambda = (N+1)\Delta\lambda \approx N\Delta\lambda . \tag{3.64}$$

That is

$$N \approx \frac{\lambda}{\Delta\lambda} . \tag{3.65}$$

Substitute (3.65) to (3.63), the longitudinal coherence length can be derived as

$$L_L = \frac{1}{2}\frac{\lambda^2}{\Delta\lambda} . \tag{3.66}$$

To deduce transverse coherence length, we can refer to figure 3.13. Here two waves A and B have the same wavelength but with slightly angular divergence $\Delta\theta$ in the propagating direction. Their wavefronts coincide at P and the transverse coherence length L_T is the length from P along the wavefront of A before it is out of phase with B. Similar to the process of deriving longitudinal coherence length, the two waves will be in phase again at $2L_T$. From figure 3.13, it can be seen that

$$2L_T\Delta\theta = \lambda . \tag{3.67}$$

Suppose the angular divergence is generated because the two waves originate from two different points on the source with a distance *D*. At an observation distance *R*, we can see that transverse coherence length can be deduced as

$$L_T = \frac{1}{2}\frac{\lambda}{\Delta\theta} = \frac{1}{2}\frac{\lambda}{(D/R)} = \frac{\lambda}{2}\frac{R}{D}. \tag{3.68}$$

To perform XPCS experiments successfully, two requirements should be satisfied. One is that the beam size or the lateral size of the illuminated sample volume should be less than L_T. The other one is that the maximum path-length difference (PLD) for x-rays in the sample should be less than L_L.

Path-length difference mainly results from beam size *d* and sample thickness *W*. As figure 3.15 shows, for beam size *d*, the maximum PLD is

$$\Delta L_d = d\sin 2\theta , \tag{3.69}$$

where 2θ is scattering angle.

For sample with thickness *W*, as figure 3.16 shows, the maximum PLD in this case is

$$\begin{aligned}\Delta L_W &= W(1-\cos 2\theta) \\ &= 2W\sin^2\theta\end{aligned} . \tag{3.70}$$

The maximum PLD can be approximately given by

$$\begin{aligned}\Delta L_{MAX} &= \Delta L_d + \Delta L_W \\ &= d\sin 2\theta + 2W\sin^2\theta\end{aligned} . \tag{3.71}$$

As mentioned previously, ΔL_{MAX} should be less than L_L at XPCS experiments.

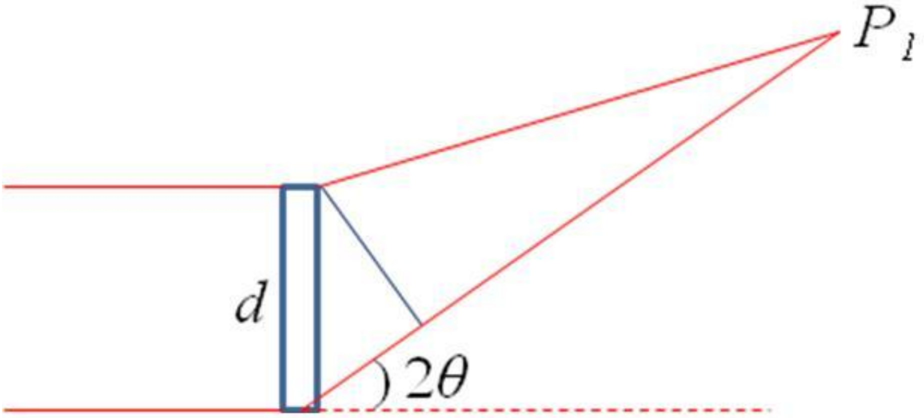

Fig. 3.15 Path-length difference from beam size *d*.

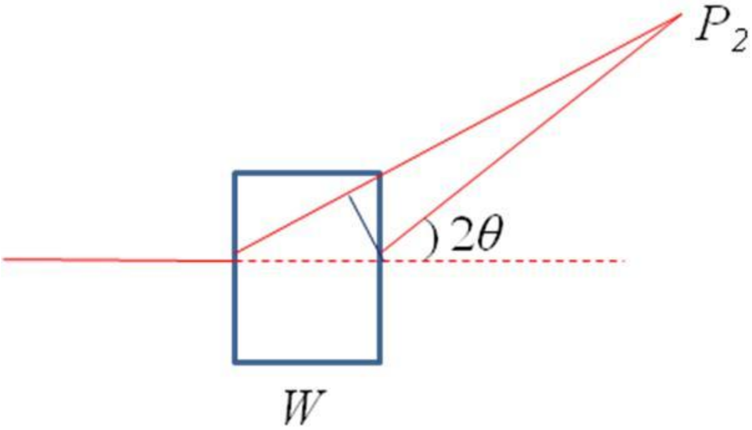

Fig. 3.16 Path-length difference from sample width *W*.

3.5.3 Application of XPCS

The typical and simple application of XPCS is to investigate the dynamics of monodisperse particles undergoing Brownian motion [42]. In the absence of interactions among the particles, the free particle diffusion coefficient D_0 of a particle with radius R is given by Stoke-Einstein relation

$$D_0 = \frac{k_B T}{6\pi\eta R}, \tag{3.72}$$

where η is the shear viscosity of surrounding medium.

$g_1(q,t)$ in this example can be reduced to

$$g_1(q,t) = \exp(-D_0 q^2 t)\,. \tag{3.73}$$

By substituting (3.73) to Siegert relation (3.62), $g_2(q,t)$ is given by

$$g_2(q,t) = 1 + \beta \exp(-2D_0 q^2 t)\,. \tag{3.74}$$

By fitting the experimental data with (3.74), we can obtain D_0. For a specific surrounding medium with known η, we can calculate the radius of the particles undergoing Brownian motion.

Here (3.73) will be derived in detail [75]. As previously derived,

$$g_1(q,t) = < \exp\{-i\mathbf{q}\cdot[\mathbf{r}(0)-\mathbf{r}(t)]\} > = < \exp[i\mathbf{q}\cdot\Delta\mathbf{r}(t)] >, \tag{3.75}$$

where $\Delta\mathbf{r}(t)$ is the displacement of the particle at time t defined as

$$\Delta\mathbf{r}(t) \equiv \mathbf{r}(t) - \mathbf{r}(0)\,. \tag{3.76}$$

$\Delta\mathbf{r}(t)$ has a Gaussian probability distribution as

$$P[\Delta\mathbf{r}(t)] = [\frac{3}{2\pi < \Delta r^2(t) >}]^{3/2} \exp[-\frac{3\Delta r^2(t)}{2 < \Delta r^2(t) >}]\,, \tag{3.77}$$

where $<\Delta r^2(t)>$ is the particle's mean-square displacement at time t given by

$$< \Delta r^2(t) > = 6D_0 t\,. \tag{3.78}$$

Finally, it can be derived that

$$\begin{aligned} g_1(q,t) &= < \exp[i\mathbf{q}\cdot\Delta\mathbf{r}(t)] > \\ &= \exp[-\frac{q^2}{6} < \Delta\mathbf{r}^2(t) >] \\ &= \exp(-q^2 D_0 t)\,. \end{aligned} \tag{3.79}$$

Besides this simple example, XPCS is also utilized to study colloid suspensions [43-45], slow dynamics in polymer system [46, 47], liquid surface dynamics [48-50] and slow dynamics in hard condensed matter systems [51-53].

4 Structure and dynamics of silica nanoparticles dispersed in 5CB

Differential scanning calorimetry (DSC), small angle x-ray scattering (SAXS), microbeam wide angle x-ray scattering (microbeam WAXS) and x-ray photon correlation spectroscopy (XPCS) have been performed to investigate the nematic liquid crystal colloid of 5CB dispersed with silica nanoparticles. In this chapter, experimental results are presented. Based on the discussion of these experimental results, a model to interpret these results is given at the end of this chapter.

4.1 Sample fabrication

Silica nanoparticles (Nippon Shokubai, Japan) were dispersed into 5CB (Wako, Japan) with the surfactant Tween 60 (Sigma-Aldrich, USA). Samples with different volume fraction of silica nanoparticles φ were fabricated, in order to investigate the dependence of structural and dynamical properties of these samples on φ.

Firstly, silica nanoparticles ($d\approx 100$ nm) were coated with surfactant (Tween 60). The procedures are shown below:

(1) Mix Tween 60 (~3.5 wt %) with water using a plastic container, heat at 80 ℃ to melt and dissolve T60, vibrate for 5 minutes with supersonic.
(2) Put silica nanoparticles into (1) and vibrate for 5 minutes with supersonic.
(3) Separate the particles from (2) with centrifuge.
(4) Wash the particles with pure water for three times.
(5) Evaporate the particles using heat plate at 80 ℃ for one hour.
(6) Collect the dried particles.

Secondly, the coated silica nanoparticles were dispersed into 5CB:

(1) Calculate the weight of particles and 5CB needed.
(2) Put the particles into a plastic container.
(3) Put 5CB into (2).
(4) Disperse at 45 ℃ for one hour with supersonic.

Thirdly, the nematic colloid was injected into the cell:

(1) Cover the rings (diameter 4 mm, thickness 1 mm) with mylar spacer on both sides.

(2) Inject the nematic colloid into the cells with injector.

4.2 Differential scanning calorimetry

Differential scanning calorimetry (DSC) is usually used to detect the phase transition of samples. Here DSC has been performed to investigate the phase transition temperatures of 5CB containing silica nanoparticles with different volume fraction.

4.2.1 Scanning parameters

DSC measurements were performed using EXSTAR 6000 (Seiko Instruments Inc, Japan). Nematic to isotropic transition temperature for pure 5CB is well known to be around 35 ℃ while its nematic to crystallization temperature is around 18 ℃ [54, 55]. The samples with silica nanoparticle volume fraction φ equal to 1.0 %, 5.0 % and 10.0 % were initially prepared at room temperature and then decreased to 10 ℃, at which the samples were kept for two minutes. Then the temperature was increased to 45 ℃ at a rate of 5 ℃/min. Samples were kept at 45 ℃ for one minute and then decreased to 10 ℃ at a rate of 5 ℃/min.

The scanning parameters are briefly illustrated by table 4.1.

Table 4.1 Scanning parameters for DSC measurements

Parameter	Step	Step	Step
	1	2	3
Initial temperature / ℃	---	10	45
Final temperature / ℃	10	45	10
Rate / ℃/min	5	5	5
Time / min	2	1	2

4.2.2 Nematic to isotropic transition temperature

Under the scanning parameters set above, DSC experiments of samples with φ equal to 1.0 %, 5.0 % and 10.0 % were performed. During the heating process, the nematic to isotropic transition temperatures were shown by figure 4.1. It can be obviously seen that the nematic to isotropic transition temperature decreases with increasing φ.

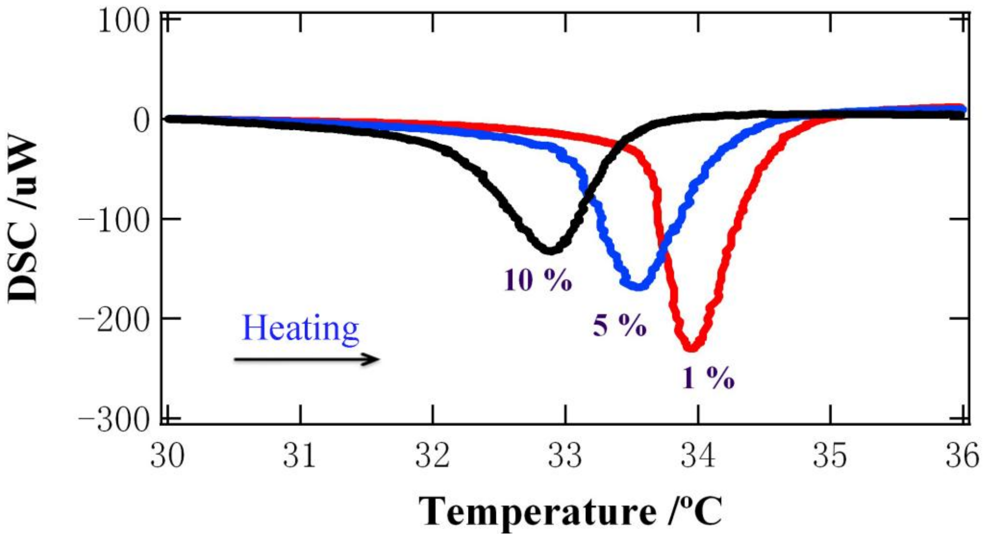

Fig. 4.1 Nematic to isotropic transition temperature during the heating process for samples with φ equal to 1.0 % (red line), 5.0 % (blue line) and 10.0 % (black line).

To interpret the dependence of nematic to isotropic transition temperature on volume fraction of silica nanoparticles quantitatively, we can refer to figure 4.2, which shows the dependence of nematic to isotropic transition temperature on φ. The black line is a linear fit of experimental data and the fitted gradient was estimated to be -0.12. The linear dependence is consistent with some previous investigations [14, 30, 33]. The shift in the transition temperature T_c is due to the elastic energy around the particles, given by

$$T_c(\phi) \sim T_0(1 - \frac{\xi^2}{R^2}\phi)\,, \tag{4.1}$$

where T_0 is the transition temperature of pure nematic liquid crystal, R is the radius of the particles, and ξ is the nematic correlation length depending on anchoring strength and nematic interaction of liquid crystal [33].

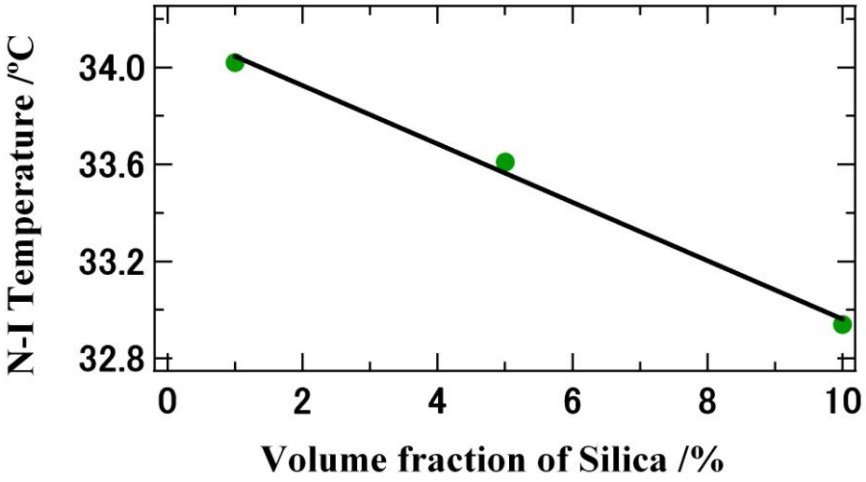

Fig. 4.2 Dependence of nematic to isotropic transition temperature on volume fraction of silica nanoparticles (green dots) and linear fit (black line).

4.3 Small angle x-ray scattering

Small angle x-ray scattering (SAXS) was performed to study the structures of silica nanoparticles dispersed in 5CB under the surfactant Tween 60. As introduced in chapter 3, SAXS can reveal average interparticle distance among the nanoparticles.

4.3.1 Experimental set up

SAXS was performed on beam line BL 03XU at SPring-8 (Hyogo, Japan). The x-ray energy was 8.3 keV, the camera length was 3 m and the detector was PILATUS (487×195 pixels, Rigaku) with a pixel size 0.172 mm. The schematic experimental setup was shown in figure 4.3. Experiments were performed at room temperature which means the 5CB should be at nematic phase.

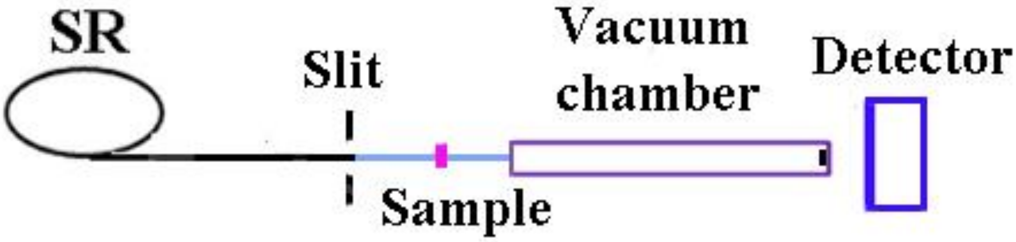

Fig. 4.3 Schematic experimental set up for SAXS at BL 03XU, SPring-8.

4.3.2 Structure factor and interparticle distance

Figure 4.4 shows the experimental scattering intensity *I* (*q*) (red line), theoretically calculated form factor *F* (*q*) (blue line) and calculated structure factor *S* (*q*) (black line). Form factor was theoretically calculated according to the scattering intensity from a single spherical particle [34]

$$F(q) \propto v^2 \frac{9(\sin qR - qR\cos qR)^2}{(qR)^6}, \tag{4.2}$$

where *v* is the volume and *R* is the radius of the spherical particle. In this experiment, *R* was given to be 50 nm.

The scattering intensity *I*(*q*) of these samples can be written as

$$I(q) \propto F(q)S(q), \tag{4.3}$$

where *F*(*q*) is form factor determined by the shape and size of the particles such as equation (4.2) in the case of spherical particle. *S*(*q*) is structure factor which reveals the interparticle structure of the particles.

From (4.3), the structure factor *S*(*q*) can be written as

$$S(q) \propto I(q)/F(q). \tag{4.4}$$

According to (4.4), by simply dividing experimental scattering intensity *I*(*q*) with theoretically calculated form factor *F*(*q*) with *R* equal to 50 nm, we can easily obtain the structure factor *F*(*q*) as the black line shows in figure 4.4.

The value of scattering intensity is different for samples with φ equal to 5.0 % and 10.0 %. However, what we focus on is not the value of scattering intensity but the peaks on structure factor profile. We found that the samples with φ equal to 5.0 % and 10.0 % showed a peak at the same q on the structure factor profile at q=0.063 nm^{-1}. The interparticle distance d can be simply calculated by the relation $d=2\pi/q$, and was estimated to be 100.3 nm. The interparticle distance 100.3 nm is in the same order as that of the diameter of silica nanoparticles, indicating that the particles contact with each other.

At low volume fractions when φ equal to 0.3 % and 0.5 %, dependence of $S(q)$ on q is shown in figure 4.5. Both of these two samples show the same peak corresponding to an interparticle distance 100.3 nm. This illustrates that even at low φ, silica nanoparticles are forced to contact with each other.

In the case of very low concentration, when the sample is very thin to be around several tens of microns, because of the short range repulsive force among the particles, there is some space between the adjacent particles [5, 21]. At high volume fraction or the sample is much thicker, the interaction between 5CB molecules and silica nanoparticles is much stronger than the repulsive interaction among silica nanoparticles, thus the silica nanoparticles are constricted to contact with each other.

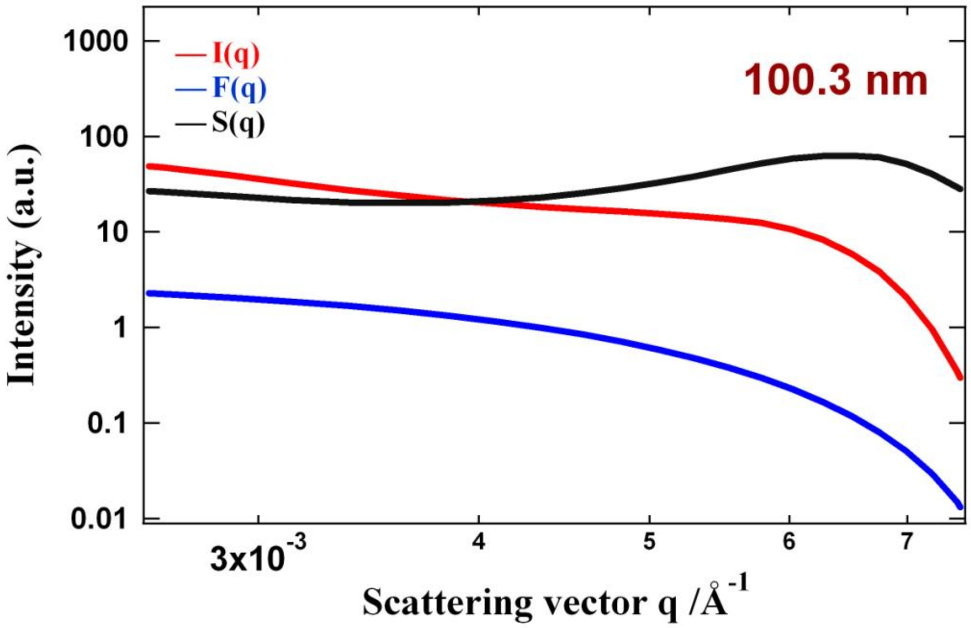

Fig. 4.4 Scattering profile of SAXS of sample with φ equal to 5.0 %. Red line: experiment scattering intensity; Blue line: theoretical form factor; Black line: calculated structure factor.

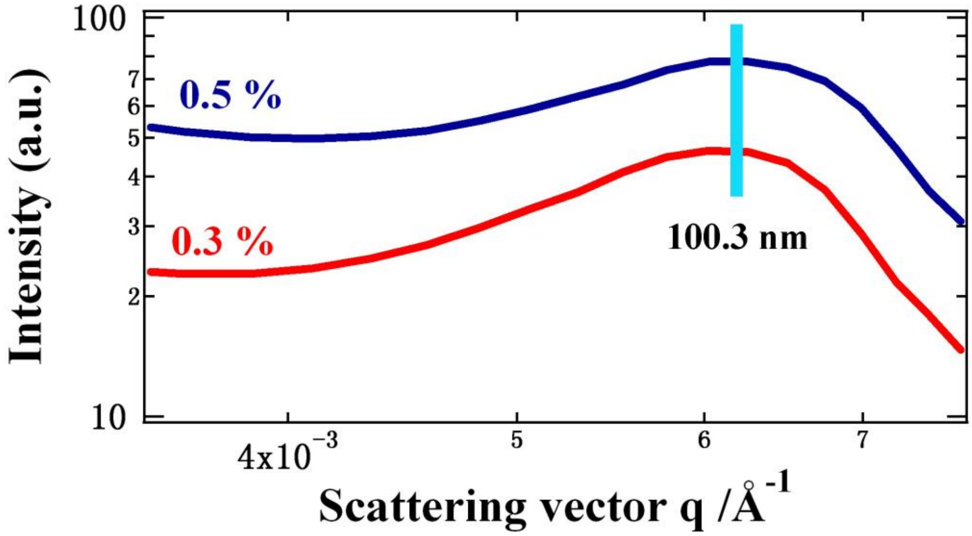

Fig. 4.5 Dependence of $F(q)$ on q for φ equal to 0.3 % (red line) and 0.5 % (blue line). The vertical bar is to clarify the peaks.

4.4 Microbeam wide angle x-ray scattering

Microbeam wide angle x-ray scattering (microbeam WAXS) can investigate the structure of 5CB molecules. By scanning the samples, the orientational change of 5CB molecules can be studied.

4.4.1 Experimental set up

Microbeam scattering was performed at BL-4A, Photon Factory (Tsukuba, Japan). The x-ray energy was 11 keV, the camera length was 12 cm and the detector was CCD (Hamamatsu Photonics Ltd., C4880-50-26A) coupled with an image intensifier (Hamamatsu Photonics Ltd.) [56]. The beam size was focused by Kirkpatrick-Baez optics [57] to 5 μm×5 μm, which enabled us to measure local structure of 5CB molecules. By scanning samples with this narrow x-ray beam, we studied the structure change of 5CB molecules as the irradiating spot changed. The experiments were performed both at room temperature and 45 ℃. Figure 4.6 shows the schematic experimental set up for microbeam WAXS.

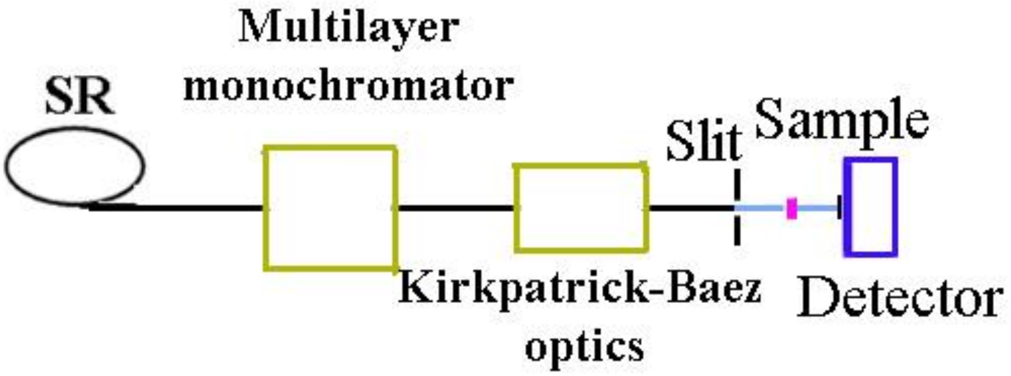

Fig. 4.6 Schematic experimental set up for microbeam WAXS at BL-4A, Photon Factory.

4.4.2 Orientation change of 5CB molecules

By scanning the samples with the narrow beam size 5 μm×5 μm, the scattering patterns from different irradiated areas were obtained. By analyzing the scattering patterns, the orientation change of 5CB molecules could be studied.

Figure 4.7 shows the scattering pattern for pure 5CB at room temperature. It can be clearly seen that 5CB is anisotropic, even though it had not been pretreated either by rubbing or by adding an electric or magnetic field. Figure 4.8

shows the scattering patterns for pure 5CB at room temperature scanned at different areas, from which we can see that the scattering patterns are almost identical within a scanning area around 1 mm×1 mm. This means 5CB is well arranged within a continuous space no less than 1 mm×1 mm, indicating that 5CB is an ideal candidate which offers a continuous nematic matrix to study the nematic colloids at room temperature. We increased the temperature to 45 ℃, and just as expected, the scattering pattern of pure 5CB becomes isotropic as figure 4.9 shows, indicating that 5CB turns to isotropic phase at 45 ℃, which exceeds its nematic to isotropic transition temperature.

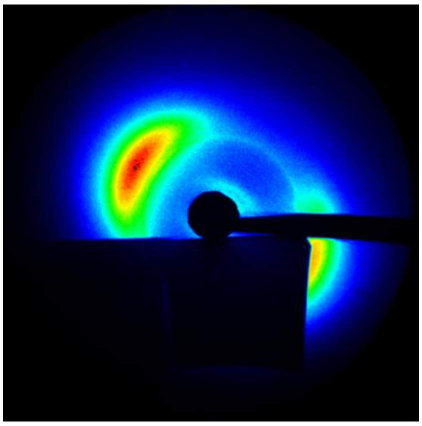

Fig. 4.7 Scattering pattern of pure 5CB at room temperature. Shadow in the center is resulted from beam stop while the quadrate shadow at the lower half is resulted from the stage holding a microscope.

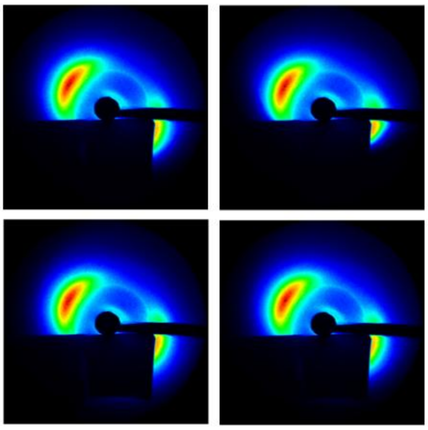

Fig. 4.8 Scattering pattern of pure 5CB at room temperature scanned at four different areas within a scanning area 1 mm×1 mm.

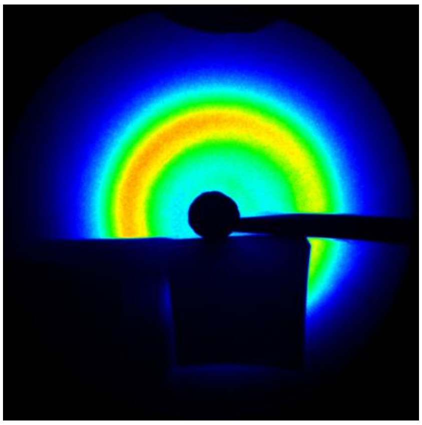

Fig. 4.9 Scattering pattern of pure 5CB at 45 ℃.

After being dispersed with silica nanoparticles, the scattering pattern of 5CB varies from that taken from pure 5CB. Figure 4.10 shows the scattering pattern of 5CB containing silica nanoparticles with a volume fraction φ equal to 0.3 % at room temperature. Four scattering patterns taken at four different areas within a scanning area 1 mm×1 mm are shown here by figure 4.10. It can be clearly seen that 5CB stays in anisotropic phase at this condition. However, the scattering patterns show different orientation, meaning that 5CB molecules undergo some orientational transition under the effect of dispersed silica nanoparticles. When temperature was increased to 45 ℃, the scattering pattern becomes isotropic as figure 4.11 shows, which indicates that 5CB turns into isotropic phase just similar to that of pure 5CB.

The scattering patterns of sample with φ equal to 0.5 % measured within the same scanning area at room temperature are shown by figure 4.12. The scattering patterns in this case are similar to that of sample with φ equal to 0.3 %. Nevertheless, within each scanning area 5 μm×5 μm, 5CB is anisotropic at low volume fraction of silica nanoparticles, which enables us to perform XPCS experiments as to be introduced later, for the beam size of XPCS experiments is also 5 μm.

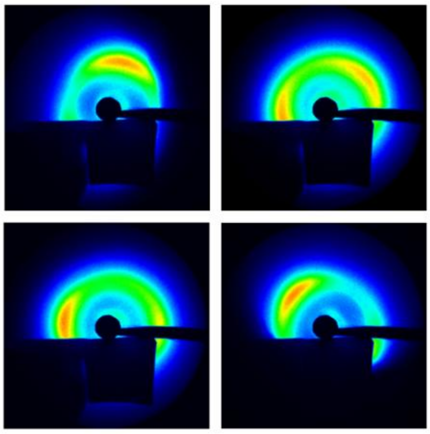

Fig. 4.10 Scattering pattern of 5CB containing silica nanoparticles with φ equal to 0.3 % at room temperature scanned at four different areas within a scanning area 1 mm×1 mm.

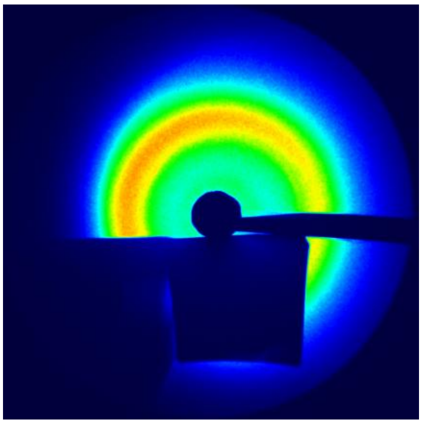

Fig. 4.11 Scattering pattern of 5CB containing silica nanoparticles with φ equal to 0.3 % at 45 ℃.

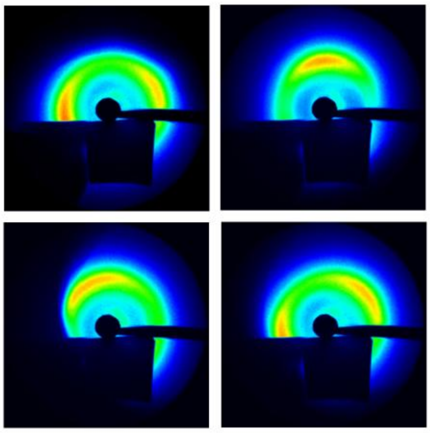

Fig. 4.12 Scattering pattern of 5CB containing silica nanoparticles with φ equal to 0.5 % at room temperature scanned at four different areas within a scanning area 1 mm×1 mm.

For 5CB containing 5.0 % silica nanoparticles, scattering pattern is remarkably changed as figure 4.13 shows. The scattering pattern becomes isotropic even at room temperature. We scanned the sample and found this isotropic pattern exists wholly within the scanning area 1 mm×1 mm as figure 4.14 shows. This transition from anisotropic to isotropic is under the effect of anchoring of 5CB molecules to the surface of silica nanoparticles.

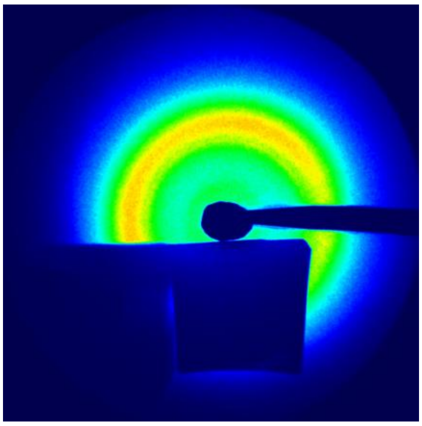

Fig. 4.13 Scattering pattern of 5CB containing silica nanoparticles with φ equal to 5.0 % at room temperature.

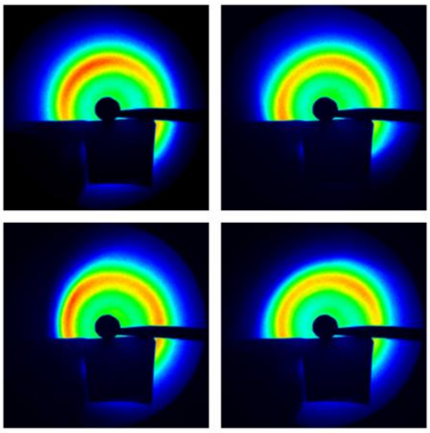

Fig. 4.14 Scattering pattern of 5CB containing silica nanoparticles with φ equal to 5.0 % at room temperature scanned at four different areas within a scanning area 1 mm×1 mm.

To quantitatively analyze the scattering patterns, two directions were defined as illustrated by figure 4.15. One is q along the radial direction and the other one is ω along the azimuthal direction.

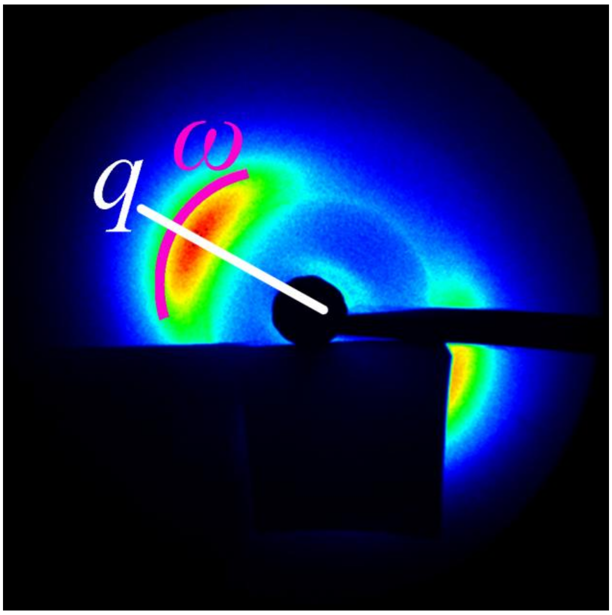

Fig. 4.15 Schematic representation of two directions: q along the radial direction and ω along the azimuthal direction.

By analyzing the full width of half maximum (FWHM) of intensity along ω, the orientation change of 5CB molecules can be studied. The data analysis process can be generally summarized as:

(1) Calculate the average intensity of each azimuthal angle (in the unit of degree);
(2) Draw the profile of the dependence of (1) on azimuthal angle;
(3) Measure FWHM of (2).

The FWHM of scattering intensity $I(\omega)$ along ω is shown by figure 4.17, from which it can be seen that FWHM increases with increasing volume fraction of silica nanoparticles.

Another method to evaluate the orientation change of 5CB molecules is also introduced here, which is called Hermans orientation parameter. Hermans orientation parameter f is to estimate the degree of orientation of molecules and it can be calculated following the procedures written here. The direction along which scattering intensity is the strongest is defined as the reference axis, and the angle θ represents the angular divergence of a direction compared to the reference axis as figure 4.16 shows [34].

$$f = \frac{3}{2} < \cos^2 \theta > - \frac{1}{2}, \tag{4.5}$$

where the averaging of $\cos^2 \theta$ is given by

$$< \cos^2 \theta >= \int_0^{\pi} \cos^2 \theta \, t(\theta) \sin\theta \, d\theta , \tag{4.6}$$

where $t(\theta)$ is pole distribution defined as

$$t(\theta) = \frac{I(\theta)}{\int_0^{\pi} I(\theta) \sin\theta \, d\theta}, \tag{4.7}$$

where $I(\theta)$ is the scattering intensity at angle θ.

By this definition, f equals to -1/2, 0 or 1 when the orientation is perpendicular to reference axis, random, or parallel to reference axis, respectively.

The calculated Hermans orientation parameter of samples with different concentration of silica nanoparticle is shown in figure 4.17. It can be clearly seen that Hermans orientation parameter decreases with increasing volume fraction of silica nanoparticle. This result coincides with the FWHM of scattering intensity $I(\omega)$ along ω, and both indicate that 5CB molecules become less orientated with increasing φ.

The fact that 5CB molecules become less oriented with increasing φ indicates an increasing influence of silica nanoparticles on 5CB. More interfaces are generated with increasing φ. The orientation change is due to the anchoring of 5CB molecules to the interfaces between silica nanoparticles and 5CB molecules.

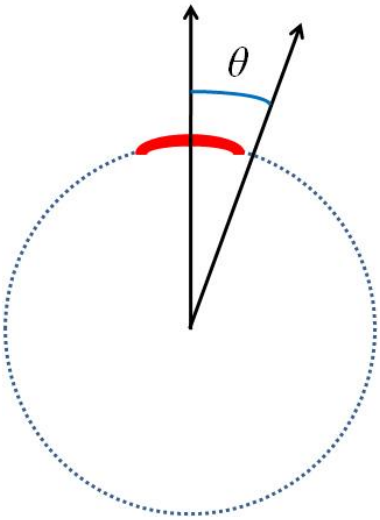

Fig. 4.16 Schematic illustration of calculating Hermans orientation parameter.

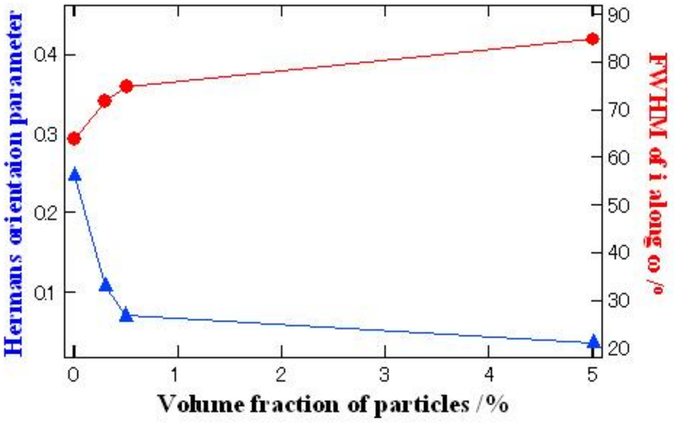

Fig. 4.17 Dependence of FWHM of scattering intensity $I(\omega)$ along ω and Hermans orientation parameter f on volume fraction of silica nanoparticles φ.

4.4.3 X-ray peak broadening

As figure 4.15 shows, we also defined a radial direction q. FWHM of scattering intensity $I(q)$ along q was calculated following the process written here:
(1) Calculate the average intensity of each scattering vector q (in the unit of $Å^{-1}$);
(2) Draw the profile of the dependence of (1) on scattering vector q;
(3) Measure FWHM of (2).

The calculated FWHM of $I(q)$ along q was illustrated by figure 4.18, from which it can be seen that FWHM increases with increasing volume fraction of silica nanoparticles φ. This phenomenon is commonly called x-ray peak broadening. Two effects are generally considered to cause x-ray peak broadening: one is grain refinement, the other one is the existence of microstress. These two effects can become stronger with increasing φ, resulting in the increase of FWHM of $I(q)$ along q.

The microstress also has an effect on the dynamics of silica nanoparticles. We can see later during XPCS data analysis that the existed microstress between 5CB molecules and silica nanoparticles can accelerate the silica nanoparticles.

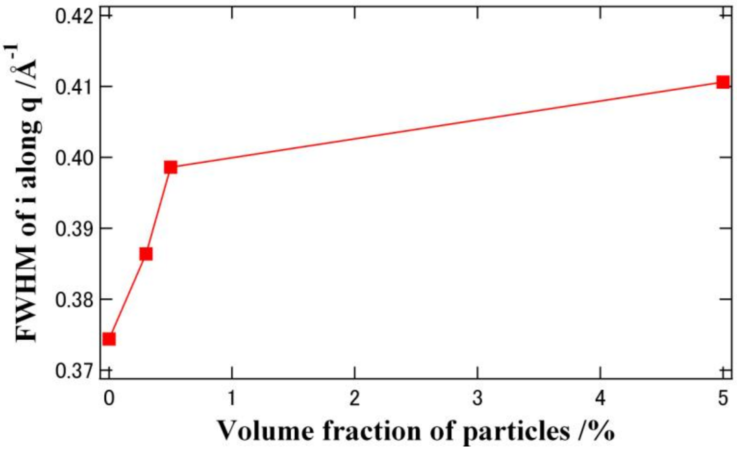

Fig. 4.18 Dependence of FWHM of scattering intensity $I(q)$ along q on volume fraction of silica nanoparticles φ.

4.5 X-ray photon correlation spectroscopy

X-ray photon correlation spectroscopy (XPCS) can investigate the dynamics of silica nanoparticles dispersed in 5CB by analyzing the normalize intensity autocorrelation function as will be introduced in this section.

4.5.1 Experimental set up

XPCS was performed on BL 40XU at SPring-8 (Hyogo, Japan). The x-ray energy was 10.5 keV, the diameter of beam was 5 μm, the camera length was 3 m and the detector was CCD (Hamamatsu Photonics Ltd., C4880-80) coupled with an image intensifier (Hamamatsu Photonics Ltd.) [56]. The schematic representation of experimental set up for XPCS is shown by figure 4.19. It has been proven that this set up can generate partially coherent x-rays and satisfies requirements to perform XPCS experiments [58]. The x-ray beam comes from helical undulator [59] and the x-rays are quasi-monochromatic even without monochromator. A high flux can be obtained from this beam line even after inserting a pinhole with a diameter of 5 μm. A second pinhole with a diameter of 35 μm was installed to remove the parasitic scattering. The experiments were performed at 29 ℃.

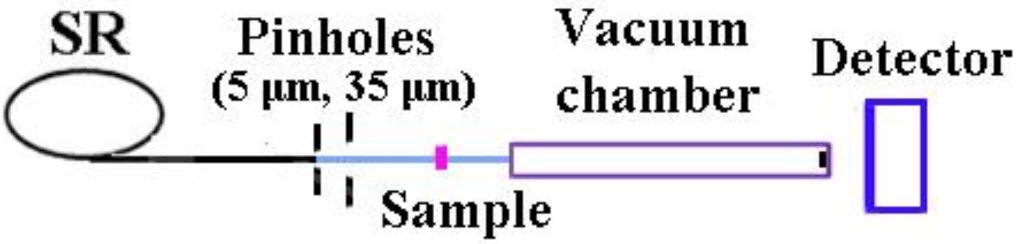

Fig. 4.19 Schematic experimental set up for XPCS on BL 40XU at SPring-8.

4.5.2 Fluctuation of scattering intensity

Actually, what we can observe directly from XPCS experiments is a so-called speckle pattern as figure 4.20 shows. Here the sample is 5CB dispersed with silica nanoparticles with φ equal to 0.5 %. Under the coherent or partially coherent light, this speckle reflects spatial disorder or inhomogeneity of the sample being irradiated [60, 61]. As we introduced in the previous section on

XPCS, the speckle pattern changes simultaneously as a consequence of the spatial arrangement change of the disordered sample.

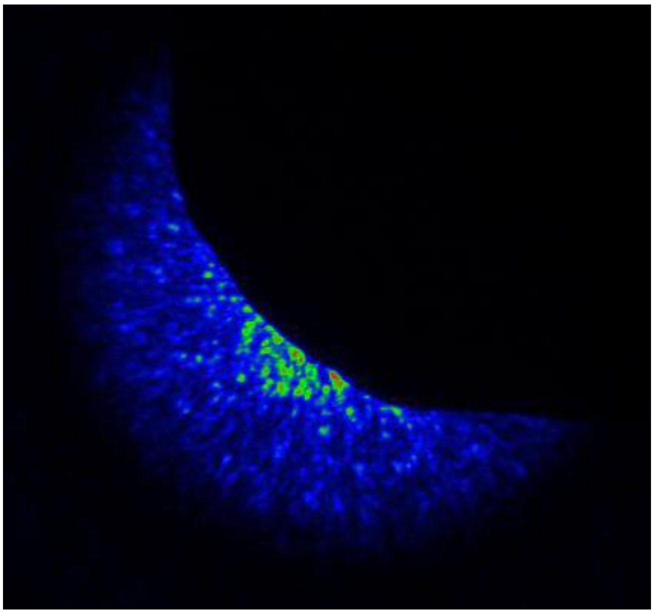

Fig. 4.20 Speckle pattern obtained from XPCS experiments.

Figure 4.21 shows the intensity fluctuation in the time sequence for the sample with φ equal to 0.3 %. The ordinate axis is around 120 adjacent pixels which locate 80 pixels from the pixel of direct beam on CCD camera, while the abscissa axis is frames taken consecutively with a short time interval in the order of several tens of milliseconds. We can clearly see that the scattering intensity fluctuates as time goes by.

Figure 4.22 and figure 4.23 shows the intensity fluctuation in the time sequence for the sample with φ equal to 0.5 % and 5.0 %, respectively. In these two cases, intensity fluctuation was also successfully observed, illustrating the change of spatial arrangement of disordered sample.

From figure 4.21 and figure 4.22, the fluctuation rate seems to be changing during the experiments, which may be resulted from inhomogeneity of silica nanoparticles within the samples.

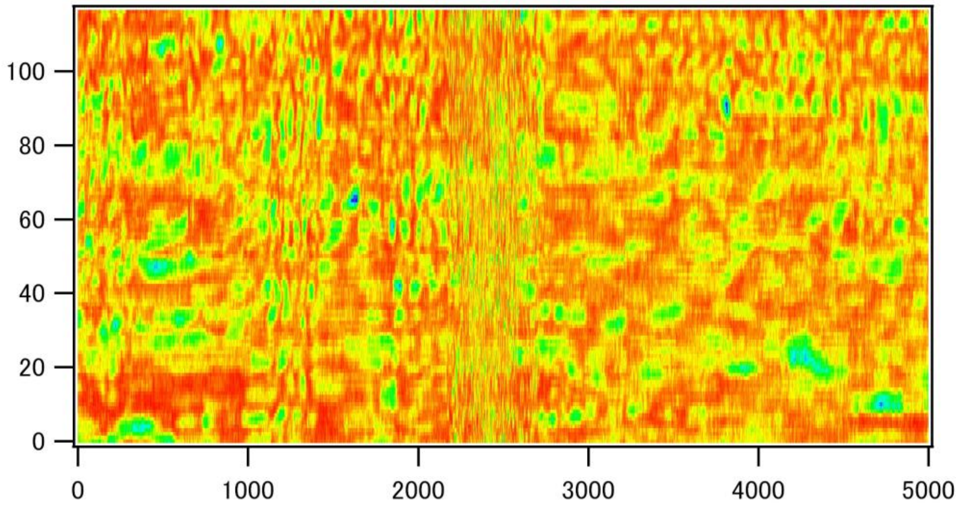

Fig. 4.21 Fluctuation of scattering intensity for sample with φ equal to 0.3 % measured at 29 ℃.

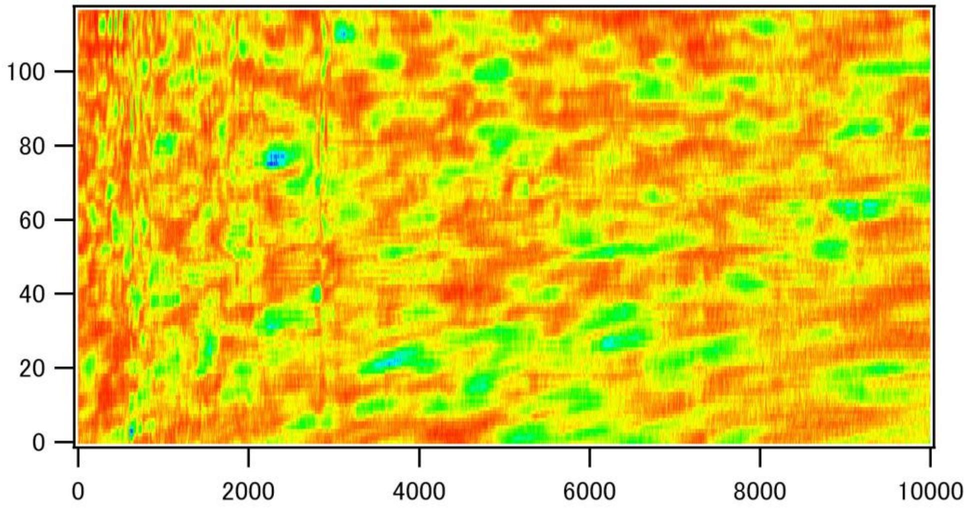

Fig. 4.22 Fluctuation of scattering intensity for sample with φ equal to 0.5 % measured at 29 ℃.

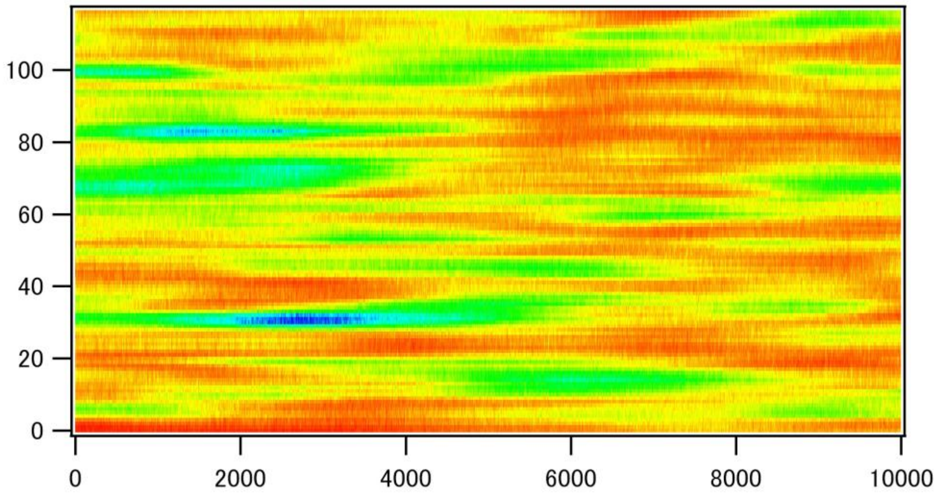

Fig. 4.23 Fluctuation of scattering intensity for sample with φ equal to 5.0 % measured at 29 ℃.

By closing watching figure 4.21 to figure 4.23, we can see the fluctuation pattern seems to be slower with increasing concentration of silica nanoparticles. To verify this, we specify the scattering intensity fluctuation at the same pixel, which locates at 50 of the ordinate axis. The result is shown in figure 4.24. Note that here the abscissa axis has been changed to time to more precisely compare the intensity fluctuation. It can be obviously seen that the intensity fluctuation of 5.0 % sample is slower than samples with φ equal to 0.3 % and 0.5 %.

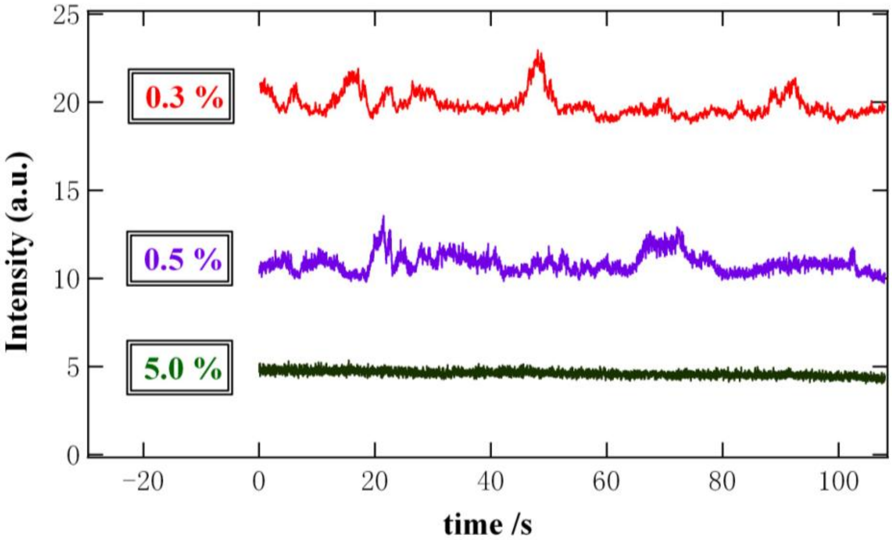

Fig. 4.24 Intensity fluctuation at the same pixel for samples with φ equal to 0.3 % (red line), 0.5 % (blue line) and 5.0 % (brown line).

4.5.3 Fitting of normalized intensity autocorrelation function

Here we will introduce the data analysis of XPCS. As we mentioned previously, the most important task in analyzing XPCS data is to calculate the normalized intensity autocorrelation function $g_2(q,t)$ and fit the function with appropriate equations. Theoretically, the data analysis process was given in chapter 3.5. Experimentally, we follow the process as introduced by D. Lumma et al [62]. Generally speaking, four steps are necessary as follows:

(1) Subtraction of dark patterns

Dark patterns are the patterns taken by CCD camera with x-rays shut off. To eliminate the effect of dark noise, the sequence of dark patterns is averaged across frames, and is subtracted on a pixel-to-pixel basis from every scattering pattern required.

(2) Correction of incident intensity fluctuation

Intensity in each pixel is divided by the scattering integrated over the entire CCD area to make a correction of incident intensity fluctuation.

(3) Calculation of intensity autocorrelation function for each pixel

In this step, the normalized intensity autocorrelation function $g_2(q,t)$ is calculated based on each pixel.

(4) Normalization for each scattering vector

For the pixels locating at the same length from the direct beam, the magnitudes of scattering vector are identical. $g_2(q,t)$ is averaged among them to obtain the intensity for the same scalar scattering vector.

$g_2(q,t)$ can commonly be fitted by an exponential equation as

$$g_2(q,t) = 1 + \beta \exp\left[-2\left(\frac{t}{\tau}\right)^{\alpha}\right], \tag{4.9}$$

where α is exponent, τ is relaxation time and β is contrast.

The calculated $g_2(q,t)$ is represented by colored marks for sample with φ equal to 0.3 % by figure 4.25. Different marks represent different magnitude of scattering vector. The yellow lines are the fitting results by equation (4.9). We can see (4.9) fits experimental $g_2(q,t)$ pretty well and gives us important parameters describing the sample investigated.

The same analysis was also done to sample with φ equal to 0.5 % and 5.0 % as illustrated by figure 4.26 and figure 4.27, respectively. In all these cases, (4.9) can fit the experimental data well. By observing the decay patterns, it can be primarily seen that the sample decays slower with increasing volume fraction of silica nanoparticles.

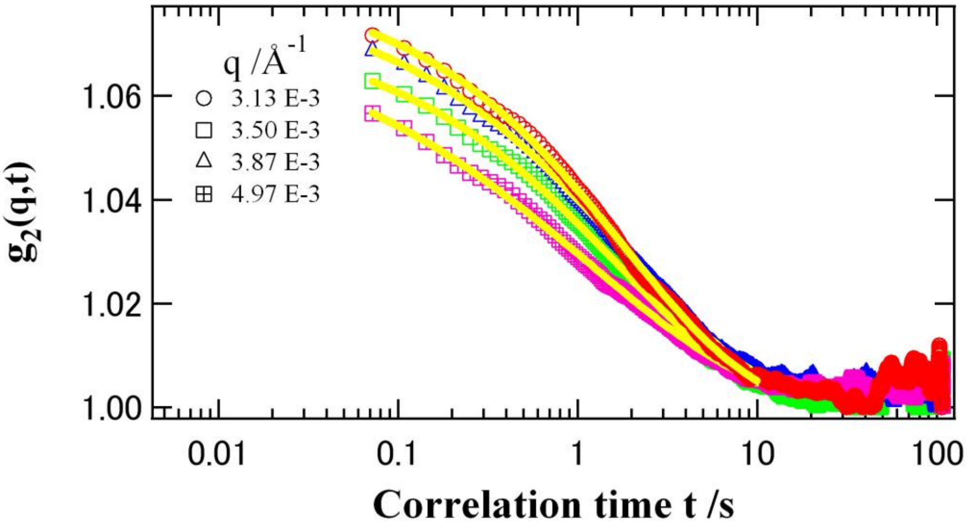

Fig. 4.25 Normalized intensity autocorrelation function $g_2(q,t)$ for sample with φ equal to 0.3 % measured at 29 ℃. Different marks represent $g_2(q,t)$ for different scattering vectors and the yellow lines are the fitted result.

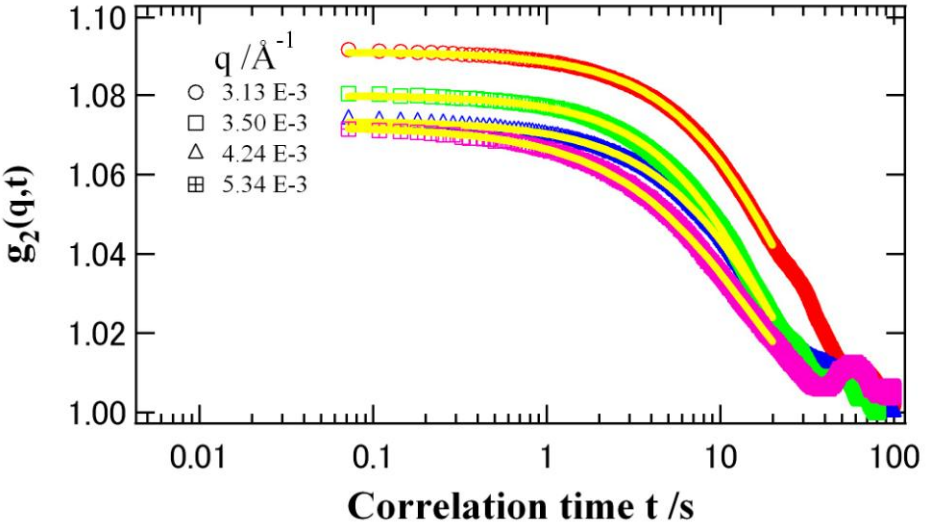

Fig. 4.26 Normalized intensity autocorrelation function $g_2(q,t)$ for sample with φ equal to 0.5 % measured at 29 ℃.

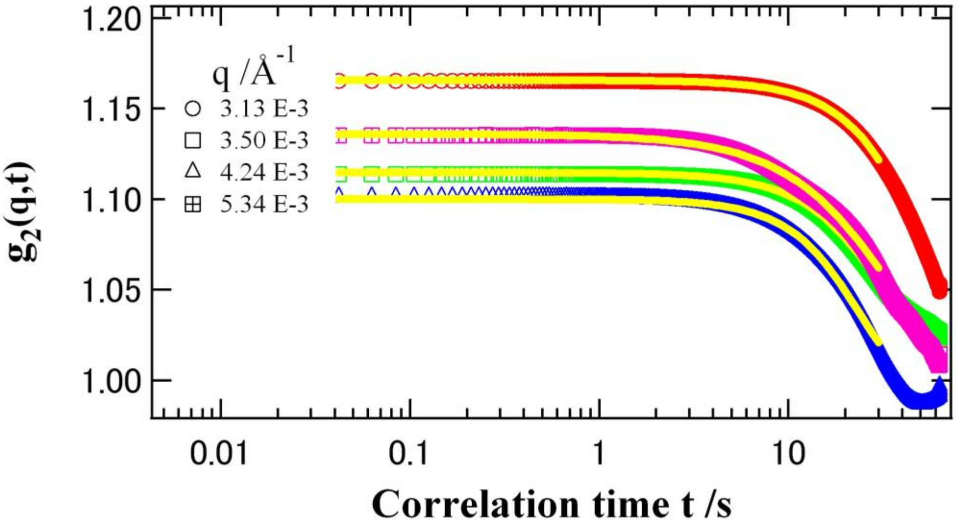

Fig. 4.27 Normalized intensity autocorrelation function $g_2(q,t)$ for sample with φ equal to 5.0 % measured at 29 ℃.

Note that there's slight deviation of fitting result from experimental data for sample with φ equal to 0.3 % as figure 4.25 shows. We think that gravity is the most possible cause for this deviation.

4.5.4 Discussion of relaxation time and component

By fitting the experimental data with the exponential equation as introduced, the relaxation time τ and component α can be easily derived. Figure 4.28 shows dependence of relation time τ on scattering vector q for samples with φ equal to 0.3 %, 0.5 % and 5.0 %, respectively. It can be obviously seen that τ increases with increasing volume fraction. All the samples have a relaxation time in the order of several seconds to several tens of seconds.

For comparison, some systems with particles dispersed in isotropic matrices are presented here. Latex was dispersed into water [63] with a volume fraction 10 % and the relaxation time of this sample is around 1 s. PMMA was dispersed into cis-decalin [64] with a volume fraction 16 % and the relaxation time of this sample is around 0.01 s. Silica were dispersed into propylene glycol [65] with the volume fraction less than 2 % and the relaxation time of this sample is around 0.1 s. In these three experiments, the relaxation times are no more than 1 s. From comparison, we can see the particles dispersed in a nematic liquid crystal have a much longer relaxation time than those in isotropic matrices, indicating the influence of anisotropy on dynamics of dispersed nanoparticles.

Figure 4.29 shows the dependence of exponent α on scattering vector for samples with φ equal to 0.3 %, 0.5 % and 5.0 %, respectively. For 0.3 % sample, α is less than unity one, indicating a stretched exponential behavior. For 0.5 % sample, α is around one, similar to a diffusive behavior as the compared systems mentioned above [63-65]. For 5.0 % sample, α is larger than one, indicating a compressed exponential behavior.

The stretched exponential behavior means that decay process is slower than Brownian motion. This phenomenon is widely observed in gels [66], glass forming materials [67], polymers [68] and colloidal systems [69]. This type of decay indicates a constrained motion, resulted from formation of clusters or branched structures, which slows down decay process and is considered to be the possible cause of stretched exponential behavior.

The compressed exponential behavior means that decay process is faster than Brownian motion. This phenomenon has been observed in gels [70, 71], polycrystals [72], clays [73] and glassy polymer melts [74]. This type of relaxation can be associated with internal stress, which creates a distribution of strain velocities. Particles are accelerated to decay faster than Brownian motion under this internal stress.

Attention should be paid that the results here are the average values, because the scattering intensity has been azimuthally averaged.

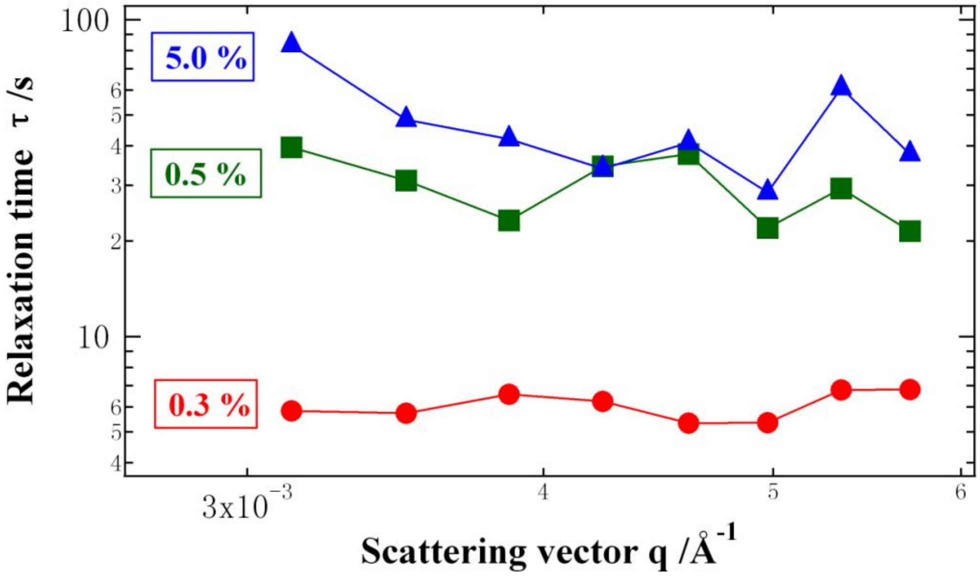

Fig. 4.28 Dependence of relaxation time τ on scattering vector for samples with φ equal to 0.3 % (red line), 0.5 % (green line) and 5.0 % (blue line).

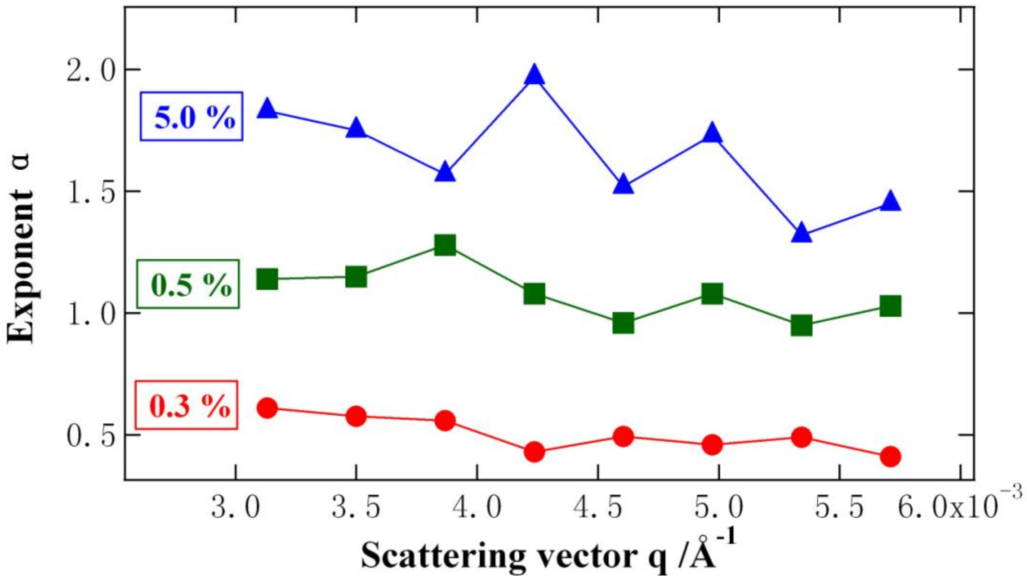

Fig. 4.29 Dependence of exponent α on scattering vector for samples with φ equal to 0.3 % (red line), 0.5 % (green line) and 5.0 % (blue line).

Microbeam WAXS shows anisotropic scattering patterns for 0.3 % and 0.5 % samples. From chapter 2 we know that nematic liquid crystal has anisotropic viscosities along different directions compared to director field. Here the normalized intensity autocorrelation function $g_2(q,t)$ was calculated along different directions as figure 4.30 illustrates. $g_2(q,t)$ was calculated at confined angular ranges 175-185 °, 195-205 °, 220-230 °, 245-255 ° and 265-275 °. If the silica nanoparticles were homogeneously dispersed in 5CB, we can expect some tendency of relaxation time on azimuthal angles, because the viscosities vary along different azimuthal angles.

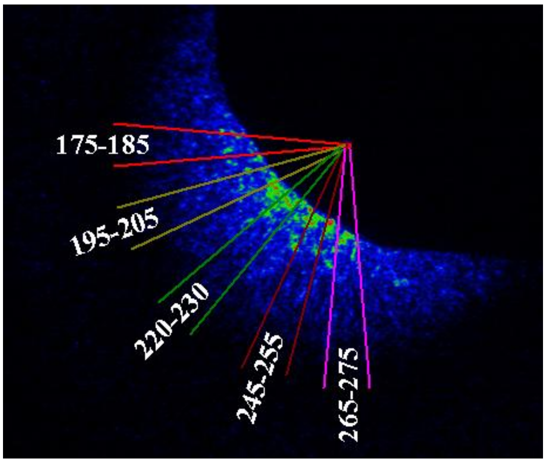

Fig. 4.30 Illustration of calculating $g_2(q,t)$ at different angles.

The calculated $g_2(q,t)$ for samples with φ equal to 0.3 %, 0.5 % and 5.0 % along different azimuthal angle were shown by figure 4.31, figure 4.32 and figure 4.33, respectively.

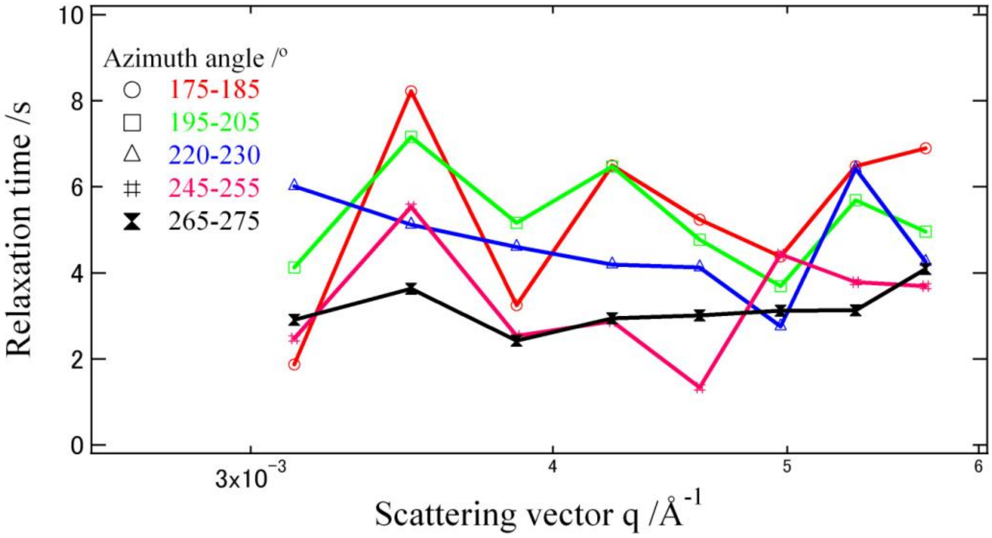

Fig. 4.31 Dependence of τ on q for 0.3 % sample calculated at different azimuthal angles.

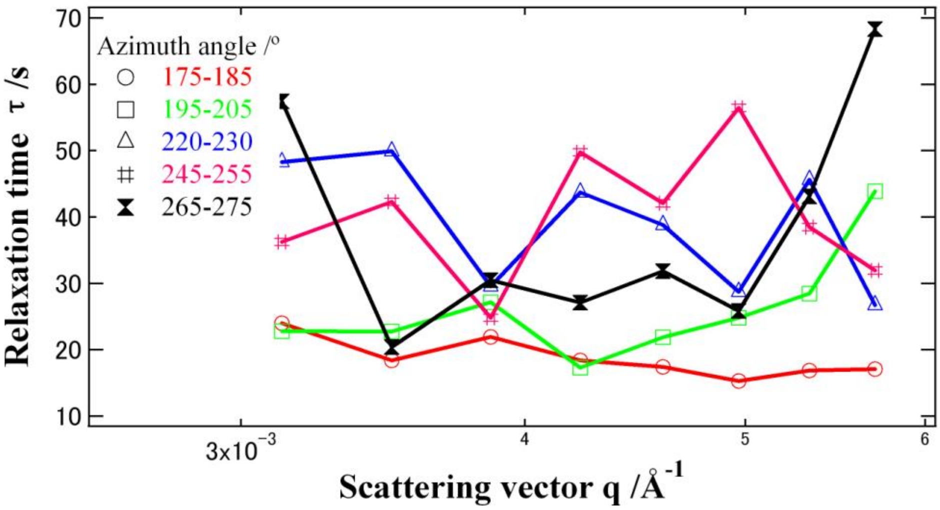

Fig. 4.32 Dependence of τ on q for 0.5 % sample calculated at different azimuthal angles.

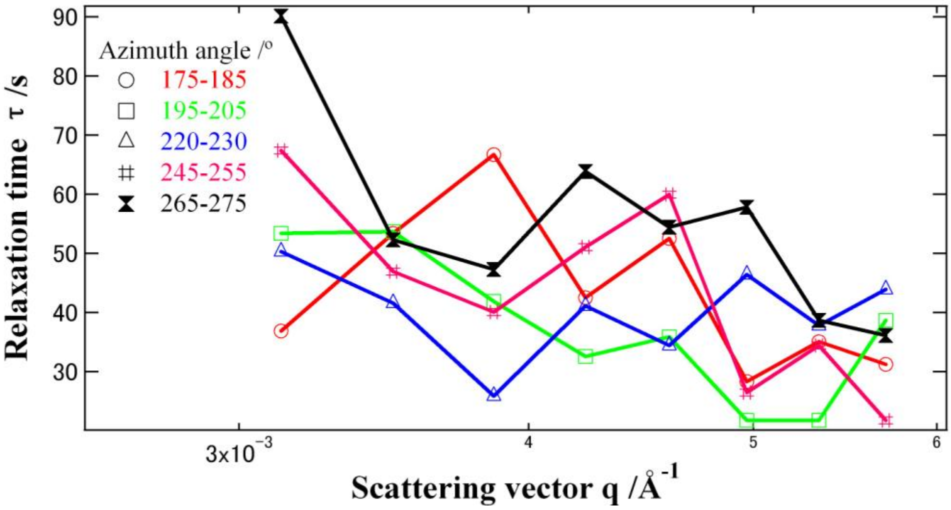

Fig. 4.33 Dependence of τ on q for 5.0 % sample calculated at different azimuthal angles.

It can be clearly seen that for each sample, curves of relaxation times obtained from various azimuth angles intercross with each other, and there’s no obvious dependence on the azimuth angles. Within the time covering the experiments, we didn’t see sedimentation of silica nanoparticles. From SAXS results, we know that silica nanoparticles contact with each other. Combining all these results together, we can say that silica nanoparticles are not homogeneously dispersed in 5CB matrices but contact with each other to form some structures which can sustain the nanoparticles in 5CB to prevent sedimentation. Formation of cellular structure is most probable. In fact, when the samples are thin to several tens of microns, cellular structure of particles dispersed in nematic liquid crystal is commonly observed under optical microscope and the size of cellular structure is in the order from several tens of microns to several hundreds of microns [14, 27-30].

The formed cellular structure of silica nanoparticles will constrict 5CB into grains. From microbeam WAXS analysis, we know that x-ray peak broadening becomes stronger with increasing φ, which may partially due to grain refinement. This illustrates that grains of 5CB become smaller with increasing φ. 0.3 % and 0.5 % samples show anisotropic scattering patterns, indicating that some 5CB molecules are oriented in grains within these two samples. For 5.0 % sample, scattering pattern of 5CB becomes isotropic, indicating 5CB molecules orient randomly in grains within this sample.

Based on above discussion, a possible model for a thin layer of sample can be given here as figure 4.34 shows. In the figures, silica nanoparticles are dispersed in 5CB as blue spheres show. The matrix is 5CB with red arrows indicating the director field around particles and green arrows indicating director field of oriented 5CB away from nanoparticles.

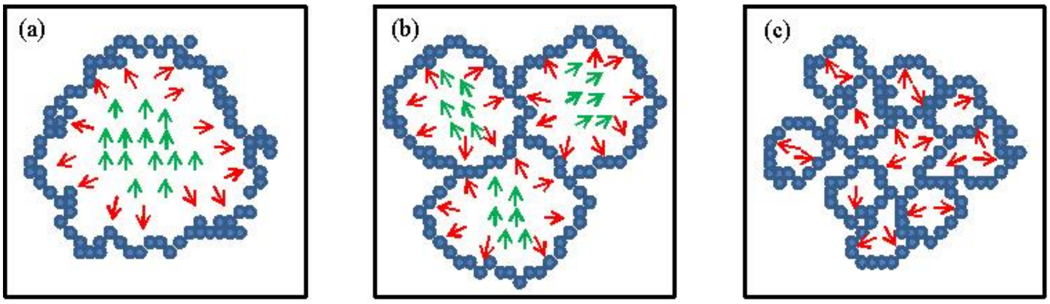

Fig. 4.34 Schematics of silica nanoparticles dispersed in 5CB. (a) 0.3 %, (b) 0.5 % and (c) 5.0 %.

At low volume fraction when φ equal to 0.3 %, silica nanoparticles are expelled away by 5CB to reduce the Frank elastic free energy and form cellular structures. 5CB molecules nearby the surface of silica will orient perpendicular to the surface under normal boundary condition of the surfactant, while the remaining 5CB away from the surface will orient along the same director to reduce the local free energy. As φ increases to 0.5 %, the cellular structure becomes smaller but inside the cellular structure, there still exist oriented 5CB molecules. When φ increases to 5.0 %, the cellular structure is further compressed and generates much more interface between silica nanoparticles and 5CB molecules, which forces 5CB molecules to orient perpendicular to the interfaces and as a consequence, the oriented 5CB domain disappears.

Under this assumption, the experimental results can be well interpreted. DSC shows that nematic to isotropic transition temperature of these nematic liquid crystal colloids decreases with increasing φ. From figure 4.34, it can be seen that with increasing φ, more silica nanoparticles are dispersed into 5CB, which results in more elastic energy. The increasing elastic energy causes more shift of the nematic to isotropic transition temperature from the case of pure 5CB [33].

SAXS shows that particles contact with each other, just as figure 4.34 shows. Silica nanoparticles are expelled away from 5CB and form a cellular structure with adjacent silica nanoparticles contacting with each other.

Microbeam WAXS shows anisotropic scattering pattern for φ equal to 0.3 % and 0.5 %, which can be well illustrated by figure 4.34 (a) and (b), where inside the cellular structures, there exists oriented 5CB molecules. For 5.0 % sample, the scattering pattern becomes isotropic, which is schematized by figure 4.34 (c), where the domains of oriented 5CB molecules disappear due to the influence of condensed interfaces between silica nanoparticles and 5CB molecules. From quantitative analysis of microbeam WAXS data, we know that 5CB molecules become less oriented with increasing φ, which is a consequence of increasing interfaces as figure 4.34 shows. To reduce surface free energy, 5CB molecules tend to orient perpendicular to the interfaces, which will cause a stronger divergence from the original director field with increasing interfaces, which is accompanying the increase of φ. X-ray peak broadening is also found to become stronger with increasing φ by quantitative analysis of microbeam WAXS data. This is as a result of two effects, the first one of which is grain refinement just as figure 4.34 shows. Grains of 5CB become smaller with increasing φ. The other effect is the increase of microstress, which compresses silica nanoparticles as well as 5CB molecules.

XPCS shows a transition from a stretched exponential behavior with φ equal to 0.3 %, to a compressed exponential behavior when φ is 5.0 %. The stretched exponential behavior is the result from the formation of clusters of silica nanoparticles [66-69] as figure 4.34 (a) shows, while the compressed exponential behavior is the result from microstress between silica nanoparticles and 5CB molecules [70-74] as figure 4.34 (c) shows.

It should be mentioned that we don't know exactly the sizes of cellular structures, because all these three samples are almost opaque under optical microscope. As previously mentioned, very thin samples with thickness around several tens of microns show that the cellular structures are in the order from several tens of microns to several hundreds of microns [14, 27-30]. Here we guess the cellular structures of our thick samples are probably of the same order.

4.6 Conclusion

Form DSC, SAXS, microbeam WAXS and XPCS experiments, several conclusions can be obtained as follows.

(1) Nematic to isotropic transition temperature of 5CB dispersed with silica nanoparticles linearly decreases with increasing φ.

(2) Adjacent silica nanoparticles contact with each other.

(3) 5CB shows anisotropic scattering pattern when φ is lower than 0.5 % and shows isotropic scattering pattern when φ is 5.0 %.

(4) 5CB molecules become less oriented with increasing φ, and x-ray peak broadening becomes stronger with increasing φ.

(5) Sample with φ equal to 0.3 % undergoes a stretched exponential behavior. Sample with φ equal to 5.0 % undergoes a compressed exponential behavior.

A schematic model to interpret these experimental results is given as figure 4.34 shows.

5 Summary

Nematic liquid crystal colloids are of great importance and have been widely studied nowadays. Colloidal particles can form anisotropic structures when dispersed into nematic liquid crystals. To fully investigate the anisotropic structures is necessary both physically and for the purpose of fabricating anisotropic materials.

Nematic liquid crystal colloids are usually translucent or even opaque, making it difficult to study these colloids with optical microscope. Actually optical microscope can only observe very thin nematic liquid crystal colloids with a thickness limited to several tens of microns.

X-rays are applicable to study opaque samples and can be a competitive implement to study these colloids. In this study, synchrotron x-ray radiation was utilized to study a nematic liquid crystal 5CB dispersed with silica nanoparticles. Small angle x-ray scattering, microbeam wide angle x-ray scattering and x-ray photon correlation spectroscopy have been performed, respectively, to study structures and dynamics of this nematic liquid crystal colloid. Some interesting results have been revealed and a schematic model based on experimental results has been proposed.

Much remains to be approached of this field, such as to confirm the mechanism underlying the transition from stretched exponential behavior to compressed exponential behavior, to investigate exactly the structure of dispersed silica nanoparticles, and to clarify the relation between structure and dynamics of nematic liquid crystal colloids.

List of figures

List of tables

Bibliography

[1] W. B. Russel, D. A. Saville and W. R. Schowalter, Colloidal Dispersions (Cambridge University Press, Cambridge, 1995).

[2] F. Mallamace and H.E. Stanley, The Physics of Complex Systems (IOS Press, Amsterdam, 1997).

[3] P. G. de Gennes and J. Prost, The Physics of Liquid Crystals (Oxford University Press, London, 1994).

[4] P. M. Chaikin and T. C. Lubensky, Principles of Condensed Matter Physics (Cambridge University Press, Cambridge, 1995).

[5] P. Poulin and D. A. Weitz, Phys. Rev. E 57, 1, 626 (1998).

[6] H. Stark, Phys. Rep. 351, 387 (2001).

[7] S. Ramaswamy, R. Nityananda, V. A. Raghunathan and J. Prost, Mol. Cryst. Liq. Cryst. Sci. Technol., Sect. A 288, 175 (1996).

[8] F. Brochard and P. G. de Gennes, J. Phys. (France) **31**, 691 (1970).

[9] P. Poulin, H. Stark, T. C. Lubensky and D. A. Weitz, Science **275**, 1770 (1997).

[10] R. Yamamoto, Y. Nakayama and K. Kim, J. Phys.: Condens. Matter **16**, S1945 (2004).

[11] R. W. Ruhwandl and E. M. Terentjev, Phys. Rev. E 5**6**, 5561 (1997).

[12] H. Stark, Eur. Phys. J. B **10**, 311 (1999).

[13] H. Stark, J. Stelzer and R. Bernhard, Eur. Phys. J. B **10**, 515 (1999).

[14] P. G. Petrov and E. M. Terentjev, Langmuir **17**, 2942 (2001).

[15] S. Chandrasekhar, Liquid Crystals, 2nd Edition (Cambridge University Press, Cambridge, 1992).

[16] M. Miesowicz, Nature **136**, 261 (1935).

[17] M. Miesowicz, Bull. Acad. Polon., Sci. Lett. Ser. A **1936**, 228 (1936).

[18] M. Miesowicz, Mol. Cryst. Liq. Cryst. **97**, 1 (1983).

[19] P. S. Drzaic, Liquid Crystal Dispersions, Series on Liquid Crystals, Vol. 1 (World Scientific, Singapore, 1995).

[20] S. Ramaswamy, R. Nityananda, V. A. Raghunathan and J. Prost, Mol. Cryst. Liq. Cryst. Sci. Technol., Sect. A **288**, 175 (1996).

[21] I. Musevic, M. Skarabot, U. Tkalec, M. Ravnik and S. Zumer, Science **313**, 954 (2006).

[22] C. P. Lapointe, T. G. Mason and I. I. Smalyukh, Science **326**, 1083 (2009).

[23] J. C. Loudet, P. Barois and P. Poulin, Nature **407**, 611 (2000).

[24] J. C. Loudet, P. Barois, P. Auroy, P. Keller, H. Richard and P. Poulin, Langmuir **20**, 11336 (2004).

[25] V. G. Nazarenko, A. B. Nych and B. I. Lev, Phys. Rev. Lett. **87**, 7, 075504 (2001).

[26] I. I. Smalyukh, S. Chernyshuk, B. I. Lev, A. B. Nych, U. Ognysta, V. G. Nazarenko and O. D. Lavrentovich, Phys. Rev. Lett. **93**, 11, 117801 (2004).

[27] J. Crain, S. P. Meeker, W. J. Hossack, R. J. Lavery and W. C. K. Poon, Mol. Cryst. and Liq. Cryst. **364**, 951 (2001).

[28] J. Cleaver, D. Vollmer, J. Crain and W. Poon, Mol. Cryst. and Liq. Cryst. **409**, 59 (2004).

[29] S. P. Meeker, W. C. K. Poon, J. Crain and E. M. Terentjev, Phys. Rev. E **61**, 6, R6083 (2000).

[30] V. J. Anderson, E. M. Terentjev, S. P. Meeker, J. Crain and W. C. K. Poon, Eur. Phys. J. E **4**, 11 (2001).

[31] M. A. Z. Ewiss, G. Nabil, B. Stoll, S. Herminghaus, Liq. Cryst. **30**, 10, 1241 (2003).

[32] S. B. Lee, K. Nakayama, T. Matsui, M. Ozaki and K. Yoshino, IEEE T. Dielect. El. In. 9, 1, 31 (2002).

[33] A. Matsuyama, J. Chem. Phys. **131**, 204904 (2009).

[34] R. J. Roe, Methods of X-ray and Neutron Scattering in Polymer Science (Oxford Univ. Press, New York, 2000).

[35] F. R. Elder, A. M. Gurewitsch, R. V. Langmuir and H. C. Pollock, Phys. Rev. **71**, 11, 829 (1947).

[36] H. Wiedemann, Synchrotron Radiation (Springer-Verlag, Berlin, 2003).

[37] A. Hofmann, The Physics of Synchroton Radiation (Cambridge Univ. Press, UK, 2004).

[38] J. A. Nielsen and D. McMorrow, Elements of Modern X-ray Physics (John Wiley & Sons, Ltd, England, 2001).

[39] Y. Nozue, Y. Shinohara and Y. Amemiya, Polym. J. **39**, 12, 1221 (2007).

[40] R. Borsali and R. Pecora, Soft-Matter Characterization (Springer, New York, 2008).

[41] D. Lumma et al, Rev. Sci. Instrum. **71**, 9, 3274 (2000).

[42] B. J. Berne and R. Pecora, R, Dynamic Light Scattering with Applications to Chemistry, Biology and Physics (Dover, New York, 2000).

[43] S. B. Dierker, R. Pindak, R. M. Fleming, I. K. Robinson and L. Berman, Phys. Rev. Lett. **75**, 449 (1995).

[44] T. Thurn-Albrecht, W. Steffen, A. Patkowski, G. Meier and E. W. Fischer, Phys. Rev. Lett. **77**, 5437 (1996).

[45] A. Robert, J. Wagner, W. Härtl, T. Autenrieth and G. Grübel, Eur. Phys. J. E **25**, 77 (2008).

[46] S. G. J. Mochrie, A. M. Mayes, A. R. Sandy, M. Sutton, S. Brauer, G. B. Stephenson, D. L. Abernathy and G. Grübel, Phys. Rev. Lett. **78**, 1275 (1997).

[47] D. Lumma, M. A. Borthwick, P. Falus, L. B. Lurio and S. G. J. Mochrie, Phys. Rev. Lett. **86**, 2042 (2001).

[48] H. J. Kim, A. Rühm, L. B. Lurio, J. K. Basu, J. Lal, D. Lumma, S. G. J. Mochrie and S. K. Sinha, Phys. Rev. Lett. **90**, 068302 (2003).

[49] A. Madsen, T. Seydel, M. Sprung, C. Gutt, M. Tolan and G. Grübel, Phys. Rev. Lett. **92**, 096104 (2004).

[50] A. Madsen, J. Als-Nielsen and G. Grübel, Phys. Rev. Lett. **90**, 085701 (2003).

[51] L. M. Stadler, B. Sepiol, J. W. Kantelhardt, I. Zizak, G. Grübel and G. Vog, Phys. Rev. B **69**, 224301 (2004).

[52] A. Malik, A. R. Sandy, L. B. Lurio, G. B. Stephenson, S. G. J. Mochrie, I. McNulty and M. Sutton, Phys. Rev. Lett. **81**, 5832 (1998).

[53] J. F. Peters, M. A. de Fries, J. Miguel, O. Toulemonde and J. B. Goedkoop, ESRF Newslett. **15**, 34 (2000).

[54] T. Mansare, R. Decressain, C. Gors and V. K. Dolganov, Mol. Cryst. Liq. Cryst. **382**, 97 (2002).

[55] T. Bouchaour, F. Benmouna, F. Roussel, J. M. Buisine, X. Coqueret, M. Benmouna and U. Maschke, Polymer **42**, 1663 (2001).

[56] Y. Amemiya, K. Ito, N. Yagi, Y. Asano, K. Wakabayashi, T. Ueki and T. Endo, Rev. Sci. Instrum., **66**, 2290 (1995).

[57] A. Iida and T. Noma, Nucl. Instr. and Meth. B **82**, 129 (1993).

[58] Y. Shinohara, H. Kishimoto, T. Maejima, H. Nishikawa, N. Yagi and Y. Amemiya, Jpn. J. Appl. Phys. **46**, 13, L300 (2007).

[59] T. Hara, T. Tanaka, T. Seike, T. Bizen, X. Marechal, T. Kohda, K. Inoue, T. Oka, T. Suzuki, N. Yagi and H. Kitamura, Nucl. Instrum. Methods Phys. Res. Sect. A **467– 468**, 165, (2001).

[60] B. J. Berne and R. R. Pecora, Dynamic Light Scattering with Applications to Chemistry, Biology and Physics (Dover, New York, 2000).

[61] M. Sutton, S. G. J. Mochrie, T. Greytak, S. E. Nagler, L. E. Berman, G. A. Held and G. B. Stephenson, Nature **352**, 608 (1991).

[62] D. Lumma, L. B. Lurio and S. G. J. Mochrie, Rev. Sci. Instrum. **71**, 9, 3274 (2000).

[63] S. Busch, T. H. Jensen, Y. Chushkin and A. Fluerasu, Eur. Phys. J. E **26**, 55 (2008).

[64] A. Fluerasu, A. Moussaid, H. Gleyzolle, P. Falus and A. Madsen, J. Synchrotron Rad. **15**, 378 (2008).

[65] A. Fluerasu, P. Kwasniewski, C.Caronna, F. Destremaut, J. B. Salmon and A. Madsen, New J. Phys. **12**, 3, 035023 (2010).

[66] C. Svanberg, T. Uematsu, P. Berntsen and P. Jacobsson, J. Chem. Phys. **126**, 051103 (2007).

[67] D. L. Sidebottom, B. V. Rodenburg and J. R. Changstrom, Phys. Rev. B **75**, 132201 (2007).

[68] R. Liu, X. Gao and W. Oppermann, Polymer **47**, 8488 (2006).

[69] D. Pontoni, T. Narayanan, J. M. Petit, G. Grubel and D. Beysens, Phys. Rev. Lett. **90**, 18, 188301 (2003).

[70] L. Cipelletti, S. Manley, R. C. Ball and D. A. Weitz, Phys. Rev. Lett. **84**, 2275 (2000).

[71] A. Madsen, R. L. L, H. Y. Guo, M. Sprung and O. Czakkel, New J. of Phys. **12** 055001 (2010).

[72] L. Cipelletti, L. Ramos, S. Manley, E. Pitard, D. A. Weiyz, E. E. Pashkovski and M. Johansson, Faraday Discuss. **123**, 237 (2003).

[73] R. Bandyopadhyay, D. Liang, H. Yardimci, D. A. Sessoms, M. A. Borthwick, S. G. J. Mochrie, J. L. Harden and R. L. Leheny, Phys. Rev. Lett. **93**, 228(2004).

[74] H. Y. Guo, G. Bourret, M. K. Corbierre, S. Rucareanu, R. B. Lennox, K. Laaziri, L. Piche, M. Sutton, J. L. Harden and R. L. Leheny, Phys. Rev. Lett. **102**, 075702 (2009).

[75] P. Lindner and Th. Zemb, Neutrons, X-rays and Light: Scattering Methods Applied to Soft Condensed Matter (North-Holland, Netherlands, 2002).